

THREE-DIMENSIONAL STRUCTURE OF THE MILKY WAY DISK: THE DISTRIBUTION OF STARS AND DUST BEYOND $0.35 R_{\odot}$

RONALD DRIMMEL

Osservatorio Astronomico do Torino, Pino Torinese, TO 10025, Italy; drimmel@to.astro.it

AND

DAVID N. SPERGEL¹

Princeton University, Princeton, NJ; dns@astro.Princeton.edu

Received 2001 January 15; accepted 2001 March 28

ABSTRACT

We present a three-dimensional model for the Milky Way fitted to the far-infrared (FIR) and near-infrared (NIR) data from the *COBE*/DIRBE instrument for Galactic latitudes $|b| < 30^{\circ}$ and to within 20° of the Galactic center. Because of the low optical depth at $240 \mu\text{m}$, the FIR emission traces the distribution of Galactic dust in the Galaxy. We model the dust distribution as due to three components: a warped exponential disk with scale length $0.28 R_{\odot}$ and a flaring scale height, a spiral arm component with four arms as traced by Galactic H II regions, and the local (Orion) arm, which produces prominent emission features at Galactic longitudes $l \simeq 80$ and -100° . A cosmic infrared background of 1.07 MJy sr^{-1} is recovered, consistent with previous determinations. The dust distribution is then used to calculate absorption in J and K , and the stellar emission in these wavebands is modeled with two components: a warped exponential disk with a scale length of $0.28 R_{\odot}$ and a spiral arm component dominated by two arms. This small scale length is consistent with a maximal disk model for our Galaxy, which is inconsistent with the cuspy dark matter halos predicted in CDM models. We find different amplitudes for the warp in the stars and dust, which starts within the solar circle.

Subject headings: dust, extinction — Galaxy: disk — Galaxy: structure — infrared: stars — infrared: ISM

1. INTRODUCTION

The detailed study of the structure of the Milky Way enables astronomers to address many of the most important questions in astrophysics, for it is only in the Milky Way that we can make detailed studies that enable us to infer the distribution of dark matter, the star formation history of the Galaxy, and the evolution of the Galaxy's spiral structure and morphology. The *COBE* satellite's all sky near- and far-infrared maps are a new window into the structure of our Galaxy and the beginning of a bridge between optical and radio observations of the Milky Way. Its potential in revealing the Galaxy lies in the greater transparency of the interstellar medium (ISM) to light at these longer wavelengths. The NIR emission arises mainly from stars, as at visual wavelengths, but probes greater distances at low Galactic latitudes, while the FIR emission is an even more powerful probe of Galactic structure as the Galaxy is nearly transparent at these wavelengths, much as in the radio regime. The FIR emission is from warm dust—the same dust that is responsible for absorption in the visual and NIR bands—and therefore uniquely traces an important component of the ISM.

Owing to extinction effects previous studies of Galactic structure based on visual Galactic emission, and typically using star count analysis, have been restricted to high Galactic latitudes, and therefore have been relatively insensitive to the nonaxisymmetric structure in the stellar distribution. However, with NIR data large-scale asymmetry in the Galactic stellar distribution begins to be clearly

revealed in a Galactic warp and the barred structure of the Galactic bulge. The existence of a Galactic warp has been known since the first radio surveys of the Galaxy, but was not seen in the stellar distribution until Djorgovski & Sosin's analysis of *IRAS* data (Djorgovski & Sosin 1989), and then later by Freudenreich et al. (1994) in the DIRBE NIR data. Meanwhile the nonaxisymmetric structure of the Galactic bulge was first revealed in the IR by Blitz & Spergel (1991), and later confirmed in the NIR from *COBE* data by Weiland et al. (1994). Since these discoveries both parametric (Freudenreich 1996; Freudenreich 1998) and nonparametric methods (Gerhard & Binney 1996; Binney et al. 1997) have been applied to *COBE* data to characterize these nonaxisymmetric features.

The Galactic bar and warp are now recognized features of our Galaxy, yet another endemic nonaxisymmetric feature of disk galaxies is spiral structure. In our Galaxy these are perhaps best mapped by H II regions (Georgelin & Georgelin 1976) and CO emission. In this contribution we apply parametric models to both FIR and NIR *COBE* data in order to describe the nonaxisymmetric structure in our Galaxy beyond $r = 0.35 R_{\odot}$.

Other than the studies already mentioned above, the IR and FIR data has also been modeled (after the removal of stellar emission in the IR by an assumed stellar emission model) by decomposing the emission into two to three components, each associated with a different gas phase of the ISM, taken to be correlated to H I, CO, and H II radio fluxes (Sodroski et al. 1997, and references therein). Applying a dust emission model to the recovered spectra then allows physical state variables of the dust to be inferred. This approach efficiently allows the removal of the Galactic foreground emission to recover the cosmic infrared background

¹ Keck Distinguished Visiting Professor of Astrophysics, School of Natural Sciences, IAS, Princeton, NJ.

(CIB) and sheds light on dust properties, but it does not yield a detailed map of the dust distribution; the decomposition procedure is limited to describing gross radial variations of dust properties, in part because of the kinematic distance ambiguity within the Solar Circle.

In contrast to the above approach, we use a parametric model to characterize the spatial distribution of the dust, making as few assumptions as necessary regarding microscopic dust properties. First efforts in this direction can be found in Spergel, Malhotra, & Blitz (1996) and Davies et al. (1997), who both compare the *COBE*/DIRBE FIR data with the predicted emission from axisymmetric models of the dust distribution. Here we employ a more complex model with multiple flux density components including not only an (cool) axisymmetric disk, but also (warm) non-axisymmetric features needed to account for major features in the FIR emission profile of the Galaxy. We adjust the model parameters by fitting the predicted 240 μm sky emission to the 240 μm Galactic emission as seen in the *COBE*/DIRBE instrument.

Once a dust model is constructed using the FIR emission we in turn use it to account for absorption in the NIR, and apply a parametric stellar flux density model to the DIRBE *J*- and *K*-band data. Like previous Galactic stellar distribution models, we employ an exponential disk component, but with the addition of spiral arms. A Galactic warp is applied to all components. Our efforts are similar to that of Freudenreich (1998, hereafter F98), though with some important differences, particularly in the derivation of the dust distribution from FIR emission rather than from NIR absorption, as in Spergel et al. (1996). We also limit our analysis to the Galactic plane ($|b| < 30^\circ$) and exclude the Galactic center (GC) region ($|l| < 20^\circ$), thereby obviating the need to model the Galactic bar and allowing us to focus on the nonaxisymmetric structure at Galactocentric radii $r > 0.35 R_\odot$.

In the following section the data reduction is described, while in § 3 the dust and stellar models are detailed. In § 4 the results of the parameter fitting procedure are given, and § 5 then discusses the uncertainties of the parameters. The final two sections are reserved for discussion of our results in light of previous work, and summarizes our conclusions.

2. DATA

In this work, we analyze the “Zodi-subtracted Mission Average (ZSMA)” maps produced from the DIRBE data by Kelsall et al. (1998) for the 240 μm band in the FIR, and the *J* and *K* bands in the NIR. The initial data set consists of a total of 393,216 pixels in each waveband on a projected cube. Full sky maps of this data are shown in Arendt et al. (1998). The data reduction procedures discussed below were done using the UIDL data analysis package developed by NASA’s Goddard Space Flight Center, as well as additional IDL code developed to work in the UIDL environment.

From the NIR bands the point sources are first removed by applying a median filter to the data, without smoothing, to identify and reject point sources (pixels with much higher intensities than neighbors) and questionable data points (pixels with much lower intensities than neighbors). Using a 5×5 pixel window a local median intensity is found at each pixel location, and pixels are kept whose intensity is between 0.5 and 1.5 times the local median. This procedure was applied to each NIR waveband separately, but any pixel rejected in one NIR band was rejected from the other

NIR band as well. A local estimate of the uncertainty, or error, σ_λ , is made at each pixel location in each waveband ($\lambda = J, K$), via the standard deviation of the emission of nonrejected pixels in a 7×7 pixel window. The estimated error for the *J* band is shown in Figure 1 with respect to Galactic latitude. The *K*-band error map is similar.

Unlike the NIR emission, which comes primarily from unresolved point sources, the FIR emission is inherently diffuse and possesses structure at all angular scales. As a result the emission locally appears as diverse features such as “ridges” and “peaks.” This necessitates that a different procedure be used to evaluate the local error. In addition, because the signal to noise is much lower in the 240 μm band than in the NIR bands, pixels are found with negative intensities after Zodiacial light removal. These values are obviously unphysical, but we want to simply exclude these data, as doing so would introduce a bias by effectively adding a net positive flux. Some smoothing is required, but with care so as to not systematically redistribute flux near the Galactic plane (GP), where the gradient of the emission is high.

At each pixel location a second-order two-dimensional polynomial is fitted to the FIR emission in a 7×7 pixel region. The value of the resulting fit at the central pixel location is taken as the smoothed value, while the standard deviation of the residuals in the window is used as an estimate of the local uncertainty, σ_{240} . This procedure introduces minimal smoothing with less noise than the data; no negative intensities are present in the smoothed data, and the total smoothed flux is equal to the total observed flux to two parts in 10,000. It is to this smoothed data that our model of the dust emission is fitted. Figure 2 shows a map of σ_{240} and the ratio of the smoothed to raw data, demonstrating that no redistributed flux associated with the GP is present in the smoothed data.

Here some words concerning the purpose of a local estimation of the error are appropriate.

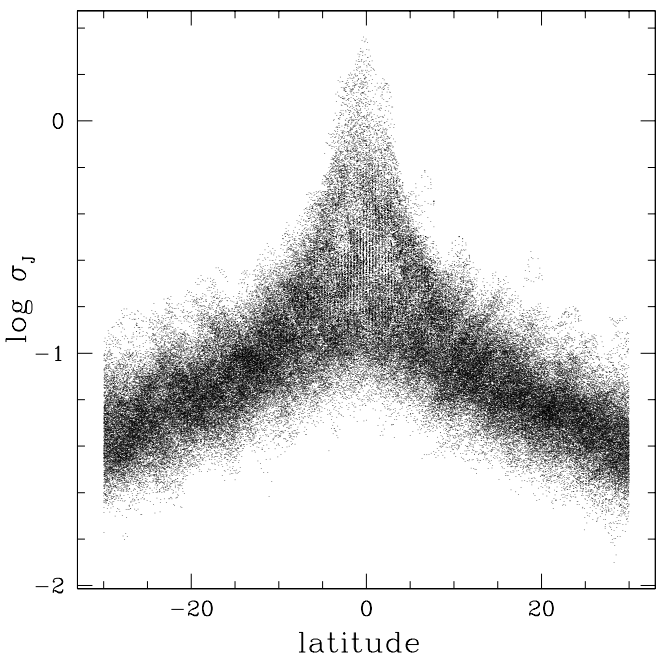


FIG. 1.—Local error in the *J* passband, with respect to Galactic latitude, evaluated at each pixel location within a 7×7 pixel window.

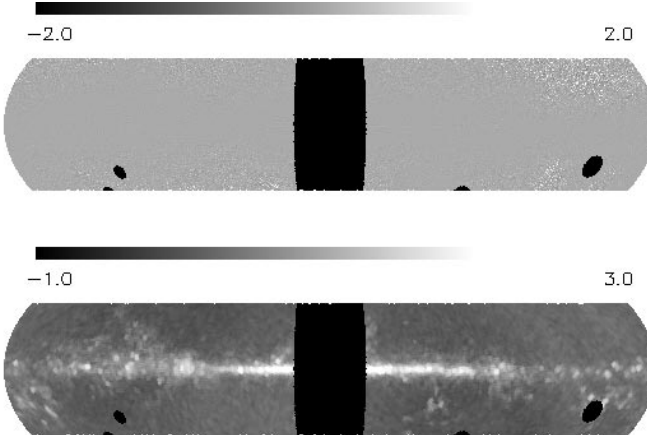


FIG. 2.—Map of the ratio of the smoothed to unsmoothed data (top), and the estimated local error σ_{240} (bottom). The maps are Mollweide galactic projections for $|b| < 30^\circ$, on logarithmic scales, indicated by the gray-scale bars. Blanked pixels are regions excluded from the present analysis (see text). Positive Galactic longitudes are to the left of center.

The local errors are used in the calculation of the merit function used in the parameter fitting procedure to be discussed below (see § 4). With *COBE*'s large beam and its high sensitivities, we are in the “confusion” limit where stars just below our detection threshold and small-scale structures in the ISM are the dominant source of “noise.” By using local deviations from a local fit or local mean as a measure of the error, an empirical estimate is being made of how “noisy” the data is in each direction. This noise is due not only to instrumental or measuring error but also includes those variations arising from (often unresolved) structure on a scale smaller than the model intends to describe. In this sense “uncertainty” is a much better descriptor than “error.” For the NIR bands the primary source of uncertainty is unresolved stars, while in the FIR the uncertainty arises from both unresolved and resolved structure. In the merit function those pixels with higher error are given less weight than those with smaller error, and are thus allowed to deviate further from the model.

Finally, as we are primarily interested here in the distribution of stars and dust in the Galactic disk, all data with $|b| > 30^\circ$ are excluded. Also excluded are pixels with longitudes within the 20° of the GC, the Orion Nebula, and regions centered on the extragalactic sources Andromeda, M33, and the Magellanic Clouds. This leaves a total of 173,569 pixels in the $240\text{ }\mu\text{m}$ data set, while after point source removal there are 152,371 pixels remaining in each NIR band, thus giving a total of 478,311 data points for the adjustment of the parameters.

3. THE MODEL

3.1. Preliminaries

Of the wavelengths at our disposal, the FIR bands provide the most direct indication of the distribution of Galactic dust, whereas the NIR bands reflect the stellar distribution and give evidence of the dust distribution through both absorption and emission features. We first consider the nature of the FIR measurements before turning to the details of the model.

The $240\text{ }\mu\text{m}$ emission, after Zodiacial light has been subtracted, is due to Galactic dust and isotropic extragalactic emission. Using the same approach as Spergel et al. (1996),

we ignore self-absorption or scattering at $240\text{ }\mu\text{m}$ as the optical depth is much less than 1 through the Galactic disk. The emission in any particular direction is then proportional to the dust column density along the line of sight and the dust's emissivity. Explicitly, the received specific intensity from a line of sight due to Galactic FIR emission is

$$I_v(T) = \int_0^{\infty} \rho(s) \epsilon_v(T) ds , \quad (1)$$

where ρ and ϵ_v represent the dust density and temperature dependent specific emissivity, respectively. However, the actual quantity represented in the sky maps from the DIRBE instrument are inferred specific intensities based on the assumption that I_v is constant. If the actual spectrum is otherwise then a color correction term is needed to relate the inferred intensities to the actual intensities:

$$D_b = I_b K_b , \quad (2)$$

where K_b is the correction term and I_b and D_b are the actual and inferred specific intensities at the representative frequency b . The correction term

$$K_b(T) = \int \frac{I_v}{I_b} W_b(v) dv , \quad (3)$$

$W_b(v)$ being the normalized frequency response of the instrument for the b passband (Hauser et al. 1999).

If the intensity arrives from a component with a single temperature, then from equations (1) and (2)

$$D_b = \epsilon_b(T) K_b(T) \int \rho(s) ds = \epsilon_b(T) K_b(T) n , \quad (4)$$

with n being the dust column density. If a sum of single temperature components are present then

$$D_b = \sum_i \epsilon_b(T_i) K_b(T_i) n_i = \sum_i k_b(T_i) n_i , \quad (5)$$

where

$$k_b(T_i) = \frac{\epsilon_b(T_i) K_b(T_i)}{\epsilon_b(T_0) K_b(T_0)} \quad (6)$$

are relative emissivities, with the (unknown) constant $\epsilon_b(T_0) K_b(0T)$ being absorbed into the column densities n_i . This constant remains unknown as long as T_0 and $\epsilon_v(T)$ remain unspecified. Indeed, if such a model for the emissive medium is assumed (as in the earlier work of Spergel et al. [1996]), it is sufficient to define $k \equiv 1$ for one of the components to proceed, letting the absolute temperature and specific emissivity of the medium remain unknown.

In the case where the temperature is spatially varying a more complicated treatment is necessary. From equations (1)–(3)

$$\begin{aligned} D_b &= \int I_v W_b(v) dv = \int \rho(s) \int \epsilon_v(T) W_b(v) dv ds \\ &= \int \rho(s) \epsilon_b(T) K_b(T) ds , \end{aligned} \quad (7)$$

where we have defined a new (local) color correction term

$$K_b(T) = \int \frac{\epsilon_v(T)}{\epsilon_b(T)} W_b(v) dv . \quad (8)$$

This new color correction term is spatially varying inasmuch as the temperature varies spatially, but will be equiva-

lent to the previous color correction term (eq. [3]) if the temperature is spatially invariant.

If it is assumed that the dust emissivity $\epsilon_v \propto v^2 B_v(T)$, where $B_v(T)$ is the Planck function, then we can define a relative emissivity,

$$k_b(T) = \frac{B_b(T)K_b(T)}{B_b(T_0)K_b(T_0)}, \quad (9)$$

and write

$$D_b = \int \rho(s)k_b(T) ds, \quad (10)$$

absorbing the constant $B_b(T_0)K_b(T_0)$ into the normalization of ρ .

It is important to point out that there is an inherent ambiguity in scale when confronted solely with a two-dimensional intensity sky map, which arises from the integrated flux column density of three-dimensional emitting structures. For arbitrary distributions of emitting matter, the relative size and flux density are mutually indeterminate; a given distribution will result in an intensity map identical to another with twice the size and half the flux density. Therefore dimensionless units are used in the model by setting $R_\odot \equiv 1$, effectively fixing the relative scale of the disk and spiral arm components of our model.

In what follows (r, ϕ, z) represent Galactic cylindrical coordinates, ϕ being taken in the direction of Galactic rotation and with the Sun lying along $\phi = 0$ at $(R_\odot, 0, Z_\odot)$. The transformations used to go from heliocentric Galactic coordinates (l, b, s) to Galactocentric Cartesian coordinates are

$$\begin{aligned} x &= R_\odot - s \cos(b) \cos(l), \\ y &= s \cos(b) \sin(l), \\ z &= s \sin(b) + Z_\odot. \end{aligned} \quad (11)$$

We are now prepared to describe the model of the dust distribution.

3.2. Dust Emission Model

The inferred specific intensity from Galactic dust emission is modeled as arising from three density components, plus an isotropic contribution:

$$D_{240}^{\text{mod}}(l, b) = \int_0^\infty (k_d \rho_{\text{axi}} + k_a \rho_{\text{arm}} + k_{+,-} \rho_{\text{loc}}) ds + Q_{240}, \quad (12)$$

where each component has an associated relative emissivity $k_j, j = d, a, +, -$. Q_{240} is an offset applied to account for isotropic extragalactic flux, i.e. the cosmic infrared background (CIB).

The earlier work of Spergel et al. (1996) described the dust density with an axisymmetric exponential disk and implicitly assumed a constant emissivity (i.e. temperature); similarly, an exponential component is employed here with the form

$$\rho_{\text{axi}} = \rho_0 \exp(-r/h_r) \operatorname{sech}^2(z/h_d), \quad (13)$$

where h_r and h_d are the scale length and height respectively. However, the scale height of the disk is given a linear flair, so that

$$h_d(r) = \begin{cases} h_{0,d} + h_{1,d}(r - r_f) & r > r_f, \\ h_{0,d} & r \leq r_f. \end{cases} \quad (14)$$

A hole is effected in the dust disk by taking $\rho_{\text{axi}} \rightarrow \rho_{\text{axi}}(r = 0.5 R_\odot) \exp[-(r - 0.5)^2/0.25^2]$ for $r < 0.5 R_\odot$. No inner dust ring is employed in the model.

For the disk component we assume a linear radial temperature gradient of $-6.8 \text{ K}/R_\odot$ with a central (reference) temperature of $T_0 = 26 \text{ K}$ and minimum temperature of 3 K . This temperature profile approximates that of the dust associated with neutral hydrogen, as found by Sodroski et al. (1997). From equation (9) $k_d(T)$ is computed, using the fitted polynomial of Schlegel et al. (1998) for $K_b(T)$, consistent with the assumption that the dust emissivity is well described by $\epsilon_v \propto v^2 B_v(T)$ (Draine & Lee 1984; Dwek et al. 1997). For the range in temperatures assigned to the disk, the emissivity is approximately linear with temperature out to $1.5 R_\odot$ (see Fig. 3).

To this exponential disk component two additional single temperature components are added, being needed to describe both prominent FIR emission and NIR absorption features, namely, the spiral arms of the Galaxy and a local feature, described as a spiral arm segment. Their respective emissivities are adjusted and relative to $k_d(T_0)$.

For the spiral arms the geometry of Georgelin & Georgelin (1976) is adopted, as implemented by Taylor & Cordes (1993), who map out four major spiral arms based on the location of H II regions. The density profile across an arm is Gaussian, with a half-width $w_a \propto r$ in the GP, and a flaring scale height h_a . For any given position in the Galaxy the nearest point of the i th spiral arm can be found numerically, with the corresponding minimum distance d_i , $i = 1, \dots, 4$. (The enumeration of the arms follows that of Taylor & Cordes.) The contribution of the spiral arm component to the density is taken to be from that arm for which the quantity $\exp(-(d_i/w_a)^2)$ is a maximum. We then have

$$\rho_{\text{arm}} = \rho_a g_a \exp(-(d_i/w_a)^2) \exp^{-(z/h_a)^2}, \quad (15)$$

where ρ_a is the density normalization for the arms and g_a describes the radial cutoff of the density along the center of

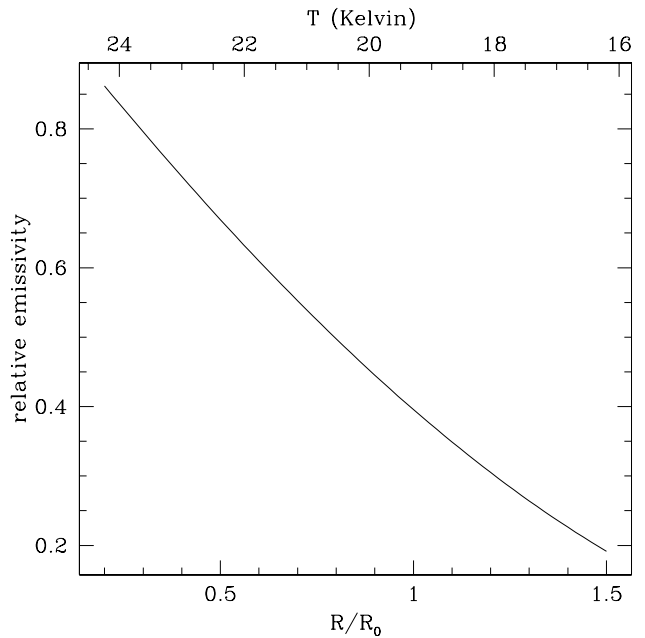


FIG. 3.—Relative emissivity of the dust disk as a function of temperature Galactocentric radius.

the spiral arms, taken to be

$$g_a(R_a) = \begin{cases} \exp [-(R_a - r_m)^2/r_a^2] & R_a > r_m, \\ 1 & R_a \leq r_m. \end{cases} \quad (16)$$

R_a being the Galactocentric radius of the nearest point of the spiral arm. The scale width and height of the arms, w_a and h_a , are functions of R_a ; the width is assumed to be proportional to Galactocentric radius ($w_a = c_a R_a$) and the scale height of the arms is given a quadratic flair:

$$h_a(R_a) = \begin{cases} h_{0,a} + h_{1,a}(R_a - r_{f,a})^2 & R_a > r_{f,a}, \\ h_{0,a} & R_a \leq r_{f,a}. \end{cases} \quad (17)$$

To the description of the spiral arms we add a final refinement, namely a reduction factor f_r on the size (c_a and h_a) of the $i = 3$ (Sag-Car) spiral arm. The need for such a reduction factor can be seen immediately from the emission profile in the GP; the inequality of the emission peaks at $\pm 50^\circ$ longitude, arising from tangent points approximately equidistant from the GC, show that the $i = 2$ and 3 arms are not equal.

The inner spiral arms account for emission features within $|l| \lesssim 80^\circ$ near the GP, producing peaks in directions corresponding to the tangents of the arms, while the outer (Perseus) arm produces a broad emission feature from approximately $l = 90^\circ$ – 180° . However, inspection of the FIR emission profiles at low Galactic latitudes also shows two prominent features that lie at about $l = 90$ and -100° . These peaks correspond with prominent absorption features seen in the NIR data, showing them to be produced by local structure. The direction of the features corresponds to the local (Orion) “arm” first seen in the distribution of young stars. While responsible for the majority of young stars in the vicinity of the Sun, the study of H II regions by Georgelin & Georgelin (1976) showed this local “arm” to be a minor feature relative to the major spiral arms in the Galaxy.

To model this local feature a spiral segment with a Gaussian density profile is employed:

$$\rho_{\text{loc}} = \rho_s \exp (-d_s^2/w_s^2), \quad (18)$$

where $d_s^2 = (r - r_s)^2 + (z - Z_s)^2$, with $r_s = R_s \exp (-a_s \phi)$ describing the spiral segment in the GP with a pitch angle $p_s = \arctan(a_s)$, and Z_s being the height of the local arm from the warped GP. It was found necessary to place the Sun within a gap, parameterized by the azimuths of the gap boundaries, ϕ_1 and ϕ_2 . That the Sun resides in a diffuse region is also suggested by other studies of the local interstellar medium (Paresce 1984; Frisch , 1996). For computational convenience the local arm is truncated at the heliocentric distance where it becomes unresolved within a pixel. Beyond the truncation points and within the gap, d_s becomes the distance to the nearest end point of the local arm. Finally, the local arm is given a different emissivity at positive versus negative longitudes ($k_{+, -}$), as it clearly shows evidence of having different temperatures: in emission it is much more prominent at positive longitudes while its NIR absorption features at positive and negative longitudes are very similar, and the FIR color ratio (D_{140}/D_{240}) shows it to be significantly hotter at positive longitudes.

To resolve the ambiguity in scale the geometry of this local feature must be fixed with respect to the GC. This is effected by fixing one of its geometrical parameters, ϕ_1 , and adjusting the ratios (w_s/ϕ_1), (Z_s/ϕ_1), and (ϕ_2/ϕ_1). In prin-

ciple the additional information contained in the NIR absorption features associated with this local arm enables this structure to be accurately placed.

3.3. Stellar Emission Model

We assume that the NIR flux is due to stellar emission, moderated by dust absorption:

$$\frac{dI_v}{ds} + \kappa_v \rho_d I_v = \rho_* \epsilon_v, \quad (19)$$

κ_v representing the specific opacity of the dust and ϵ_v the specific emissivity of the stars. Integrating over frequency after multiplying by the passband’s frequency response function $W_b(v)$, and remembering that $D_b = \int I_v W_b(v) dv$, we arrive at the equation

$$\frac{dD_b}{ds} + \kappa_b \rho_d D_b = \rho_* \epsilon_b K_b, \quad (20)$$

where we have used the color correction factor K_b defined in equation (8), though in this context it is not a function of temperature. The densities ρ_d and ρ_* are for the dust and stars respectively, and the opacity is now a mean opacity:

$$\kappa_b = \frac{\int \kappa_v I_v W_b(v) dv}{\int I_v W_b(v) dv}. \quad (21)$$

If the stellar NIR emission is dominated by a single stellar population, possessing a characteristic specific emissivity ϵ_b (or luminosity function), then ϵ_b and K_b are spatially invariant. We therefore combine all the terms on the right-hand side of equation (20) into a stellar flux density, η_b , and arrive at

$$D_b^{\text{mod}}(l, b) = \int_{\text{los}} \eta_b(s) \exp [-\tau_b(s)] ds + Q_b. \quad (22)$$

The mean optical depth $\tau_b(s)$ is found from the dust distribution model and Q_b is an isotropic offset term, albeit here without astrophysical justification.

The optical depth $\tau_b(s)$ in equation (22) is defined as

$$\tau_b(s) = \int_0^s \kappa_b \rho_d ds'. \quad (23)$$

We then use the following approximation, treating κ_b as spatially invariant:

$$\tau_b(s) \approx \kappa_b \int_0^s \rho_d ds' = \kappa_b (A_b/A_V) \int_0^s \rho_d ds'. \quad (24)$$

We adopt the (A_J/A_V) and (A_K/A_V) ratios of Rieke & Lebofsky (1985), and leave κ_b as an adjustable parameter. Rather than using the dust column density as given by the model for calculating the opacity, we follow Spergel et al. (1996) and use a rescaled density, achieved here by applying a line-of-sight scaling factor to only one of the density components of the dust model. The scaling factor is determined by requiring that the predicted FIR emission using the rescaled density be equal to the observed FIR emission. For a given line of sight the modeled FIR emission is $D_{240}^{\text{mod}} = \sum D_j + Q_{240}$, where the sum is over the emission contributions of the three dust density components. The appropriate scaling factor for component j is then

$$f_j = \frac{D_{240}^{\text{obs}} - \sum_{i \neq j} D_i - Q_{240}}{D_j}. \quad (25)$$

For each line of sight one of the scale factors f_j is chosen and used to rescale that component's density, i.e., $\tilde{\rho}_j = f_j \rho_j$, and the total dust density ρ_d used in equation (24) is recomputed with this rescaled density. The component chosen to be rescaled is that whose scaling factor results in the smallest fractional change in the component's column density, that is, the scale factor f_j which minimizes $|1 - f_j|$. However, if the modeled intensity from the nonaxisymmetric components is at least 10% of the observed intensity then either spiral arms or the local arm is rescaled. This bias only has affect in or near the GP where the condition is satisfied. It is also required that $f_j > 0$ to be considered as a valid rescaling factor. This rescaling procedure assumes that the entire residual in the FIR intensity, $D_{240}^{\text{obs}} - D_{240}^{\text{mod}}$, is due to the modeled dust density deviating from the true density, rather than from deviations in the emissivity (i.e. temperature).

If more than one stellar population is modeled, then the right-hand side of equation (20) will consist of a sum of components, namely, $\sum_i \rho_{*,i} \epsilon_{b,i} K_{b,i} = \sum_i \eta_{b,i}$, where only the normalization of each component is waveband dependent. The stellar flux density η_b is modeled using two components, an exponential disk and a spiral arm component, both with a sech^2 vertical structure. The stellar spiral arms are assumed to have a density proportional to the disk component, so that the total stellar flux density is then

$$\eta_b = \eta_b^0 \exp(-r/r_*) [\text{sech}^2(z/h_*) + B_b g(R_a) \times \exp(-(d_i/w_a^*)^2 \exp(-(z/h_a^*)^2)]. \quad (26)$$

As for the dust, d_i is the distance in the GP to the nearest spiral arm, the half width w_a^* is proportional to R_a , the radius of the nearest point of the spiral curve, h_a^* is the scale height of the arms, assumed to be constant with Galactocentric radius, and $g(R_a)$ is a function that describes the variation in density along the arm. The parameter B_b ($b = J, K$) describes the relative amplitude of the arms; allowing this parameter to vary with waveband is equivalent to assuming that the arms consist of a stellar population that differs from that of the disk component. In addition, a stellar cutoff factor is applied for radii greater than the cutoff radius r_c :

$$f_{\text{cut}} = \exp\left(-\frac{r - r_c}{r_*/5}\right), \quad (27)$$

applied so that $\eta_b \rightarrow f_{\text{cut}} \eta_b$ for $r > r_c$.

We explore two different basic geometries for the stellar spiral arms. One is of a logarithmic form, whose phase and pitch angles are adjusted. In this case the n th arm of m logarithmic spirals has a radius

$$R_n = R_0 \exp(-a\phi) \exp\left[a \frac{2\pi}{m}(n-1)\right], n = 1, \dots, m \quad (28)$$

where a is the tangent of the pitch angle, p . For these spirals $g(R_a) \equiv 1$. Both $m = 2$ and $m = 4$ spiral geometries will be tried in § 5 against the data.

The second spiral arm geometry, adopted for our standard model, is a sheared version of the spiral model employed for the dust distribution. Under the assumption that the dust spirals show the location of star formation fronts in the Galaxy, a young stellar population may be expected to drift "downstream" from the arm by an amount described by an offset in Galactocentric azimuth. If

the arms are assumed to have a fixed pattern in the presence of a flat rotation curve, then the drift in azimuth is

$$\phi_\tau = V_o \tau \left(\frac{1}{r} - \frac{1}{R_C}\right), \quad (29)$$

where V_o is the circular rotation speed, τ the mean age of the population, and R_C the corotation radius. The above shear in azimuth is applied to the loci of the points describing the dust spirals. Because of mean color differences in stellar populations of different ages, we expect the spiral arms to have different offsets in the different wavebands. Thus we let τ vary with waveband (henceforth τ_b), as well as the width of the arms (hence $w_b^* = c_b^* R_a$). In this formulation the geometry is found by adjusting parameters equivalent to $V_o \tau_b$ and R_C . For these sheared spirals the function $g(R_a)$ is the same as for the dust, and the reduction factor on the Sag-Car arm is applied only to its width. It is this model of the spiral arms that we adopt as our standard model, shown in detail in the next section.

A global warp is added to all components by making the substitution $z \rightarrow z'$ in the above formulation, where $z' = z - Z_w$ for the dust components, or $z - Z_w^*$ for the stellar components, the function $Z_w(r, \phi)$ describing the vertical displacement of the warp. For the dust

$$Z_w = h_w(r) \sin(\phi - \phi_w), \quad (30)$$

where ϕ_w is the phase of the warp, and the amplitude function

$$h_w(r) = \begin{cases} a_w(r - r_w)^2 & r > r_w, \\ 0 & r \leq r_w, \end{cases} \quad (31)$$

with r_w being the Galactocentric distance that the warp starts, and a_w an amplitude parameter. For the stars a separate amplitude coefficient a_w^* is applied, allowing the stellar warp to have a different amplitude, similar to F98.

4. ADJUSTMENT OF PARAMETERS

In order to determine the set of parameters that yields a best fit to the data we minimize a merit function of a χ^2 form, specifically the sum of the χ^2 for each waveband:

$$\chi_b^2 = \sum \left[\frac{(D_b^{\text{mod}} - D_b^{\text{obs}})^2}{\sigma_b} \right], \quad (32)$$

the summation being over all pixels, and σ_b being the uncertainties estimated in § 2. The general nonlinear minimization routine N2FB from the PORT mathematical library, developed by AT&T Bell Laboratories, is used to minimize χ^2 .

The determination of the intensity $D_b^{\text{mod}}(l, b)$ predicted by a model entails the numerical evaluation of the line-of-sight integrals in equations (12) for the FIR and (22) for the NIR. These numerical integrations are carried out by applying the trapezoidal rule with an exponentially increasing quadrature. The exponential convergence of the integrals allow us to approximate the infinite range by integrating out to a finite number of effective scale lengths; we integrate to ten effective scale lengths in one hundred steps. Intermediate values of the line-of-sight integration through the dust are tabulated to determine the column density $\int \rho_d(s) ds$ in equation (24) to calculate the optical depth $\tau(s)$. To test the

numerical integration, comparisons were made with analytic solutions of an axisymmetric case, namely $\rho \propto \exp(-r/h_r - |z|/h_z)$, at various latitudes along the Galactic meridian ($l = 0, 180^\circ$). The results of these tests show a relative error of 2×10^{-4} .

Unfortunately, because of computational limitations and the number of parameters that must be employed to describe both the stars and the dust, a simultaneous fit to all wavebands was not possible. The fitting of the parameters is thus done in a two step process. In the first step parameters describing the dust distribution are adjusted using only the FIR data, then the remaining parameters to the NIR data.

4.1. Adjustment to the FIR

The integration of the dust model along multiple lines of sight renders an FIR intensity sky map that can be directly compared with the DIRBE 240 μm sky map. However, there are several ambiguities that the FIR data alone does not allow to be resolved. Already mentioned is the ambiguity in scale, which leads us to adopt length units such that $R_\odot \equiv 1$. A second ambiguity remains in the decomposition of the flux densities into emissivities and densities, requiring that one or the other be fixed. For the fit to the FIR emission we specify that $k_- = k_a = 1$, which are relative to the emissivity of the disk component, already defined by its assumed temperature gradient. (The requirement that the local arm has the same density and dimensions at both positive and negative longitudes adds an additional constraint that allows k_+ to be adjusted relative to k_- .)

While setting $R_\odot = 1$ defines the scale of the model, the Sun's height above the GP, Z_\odot , in principle remains a free parameter to be adjusted. However, there is a near degeneracy between Z_\odot and the other parameters that determine the latitude of the projected emission from the local arm. For this reason it was found necessary to fix Z_\odot in the FIR adjustment while adjusting the warp parameters and (Z_s/ϕ_1) . We have set $Z_\odot = 0.001875$ (15 pc/8 kpc), consistent with other estimates based on NIR data (16 pc, F98; 15.5 pc, Hammersley et al. (1995)), though smaller than recent determinations based on optical star count analysis (20.5 ± 3.5 pc, Humphreys & Larsen (1995); 27 ± 3 pc, Mendez & van Altena (1998)). However, Haywood, Robin, & Creze (1997b) point out that these later estimates are sensitive to the adopted scale height of the disk and should be adjusted downward to ~ 15 pc if a smaller effective scale height of the disk is adopted, as they advocate. It's worth noting that if the local arm is assumed to be in the GP (i.e. $Z_s = 0$), adjusting Z_\odot leads to $Z_\odot < 0$, contrary to almost all studies of Z_\odot , which place the Sun above the GP; this was the primary reason for introducing Z_s as a parameter.

A second parameter found to be poorly determined is the inner scale height of the spiral arms, $h_{0,a}$. This parameter is constrained by the emission of the inner spiral arm tangents, but these make up too small a fraction of the total emission to allow a reliable adjustment of $h_{0,a}$. We have therefore set $h_{0,a} = 0.01 R_\odot$.

A total of 22 parameters are adjusted in the FIR fit: There are four adjusted parameters associated with the disk component ($\rho_0, h_{0,d}, h_{1,d}, h_r$), seven associated with the spiral arms ($\rho_a, c_a, h_{1,a}, r_{f,a}, r_m, r_a, f_i$), seven associated with the local arm ($\rho_s, R_s, p_s, (w_s/\phi_1), (Z_s/\phi_1), (\phi_2/\phi_1), k_+$), three associated with the warp (r_w, a_w, ϕ_w) and the offset Q_{240} . Six parameters remain fixed: $\phi_1, r_f, h_{0,a}, Z_\odot$, and the emissivities k_- and k_a . The resulting parameters of the pre-

liminary dust fit are given in Table 1, expressed for convenience in units where $R_\odot = 8$ kpc.

We leave the general discussion of the implications of the parameters for later (§ 6), but here present the resulting sky map of the FIR emission produced by the model as compared with the observations. Figure 4 shows the observed and modeled 240 μm sky emission, and a map of their relative difference, $(D^{\text{obs}} - D^{\text{mod}})/D^{\text{obs}}$. Such grey scale maps give an overall impression of the emission, but do not show the variations in the GP where most of the details of interest are located. To show a more direct comparison between the modeled and observed signal, emission profiles in the GP and other Galactic latitudes are shown in Figures 5 and 6. In these emission profiles it appears that the model has higher residuals at higher latitudes. However, this is an effect of the logarithmic scale used; Figure 7 shows that the residuals are in fact smaller at higher latitudes.

The emission profiles show that the major emission features are reproduced. In the GP the emission peaks at the tangents of the spiral arms ($l \approx \pm 30^\circ, \pm 50^\circ$, and -80°), and the peaks from the local arm (at $l \approx 80^\circ$ and -100°) are correctly placed. In the sky maps the local arm shows itself as two bright spots with considerable extent in latitude in nearly opposite directions of the sky. The Galactic warp is evident in the sky maps as an asymmetry in the Galactic emission at positive versus negative latitudes. An emission feature due to the outer Perseus arm is evident as a broad feature from approximately $l = 80^\circ$ to -140° in Figure 6 for latitudes $b > 5^\circ$. This arm is seen primarily at positive latitudes due to the Galactic warp, and its large extent in latitude as compared to the inner arms is what necessitates a flaring in the scale height of the spiral arms. The warp also accounts for the small negative deviation in latitude at $l \approx -80^\circ$, a feature associated with dust within the Solar Circle.

4.2. Adjustment to the NIR

A final adjustment to the NIR data yields the remaining parameters of the stellar distribution and resolves the remaining uncertainties of the dust distribution; the additional information provided by NIR absorption, proportional to the dust column density, allows the decomposition of the dust densities and FIR emissivities. For example, fixing all other parameters of the spiral arms, the FIR flux column density from the arms arriving from any particular line of sight is simply proportional to the product $(k_a \rho_a)$. The decomposition is effected by adjusting ρ_a and varying the emissivity k_a so as to keep the product $(k_a \rho_a)$ constant, thus preserving the modeled FIR signal. Similarly for the local arm, the column flux density is fixed, while ρ_s is adjusted.

In the fit to the NIR the parameter Z_\odot is adjusted, while the distance to the warped plane, $Z_\odot - Z_w(r_\odot)$, is preserved by appropriately varying ϕ_w , leaving the parameters a_w and R_w fixed to the values found in the FIR fit. Meanwhile, the amplitude factor for the stars, a_w^* , is adjusted to allow the stellar warp to have a different amplitude than that found in the dust.

In summary there are nineteen adjusted parameters in the adjustment to the NIR data: five parameters describing with the disk component ($\eta_{J,K}^0, r_*, h_*, r_c$), seven parameters associated with the spiral arms ($B_{J,K}, c_{J,K}^*, V_o \tau_{J,K}, R_C$), three parameters associated with the dust and its absorption (κ_V, ρ_a, ρ_s), the stellar warp amplitude parameter, a_w^* ,

TABLE 1
DUST PARAMETERS

Parameter	Symbol	Value	Uncertainty
Disk component:			
Density	ρ_0	1098 MJy sr ⁻¹ kpc ⁻¹	41
Scale length	h_r	2.26 kpc	0.16
Base scale height	$h_{0,d}$	134.4 pc	8.5
Linear flair coefficient	$h_{1,d}$	14.8 pc kpc ⁻¹	9.9
Flair radius ^a	r_f	4.40 kpc	...
240 μm Offset	Q_{240}	1.07 MJy sr ⁻¹	0.15
Local Arm:			
Radius at $\phi = 0$	R_s	8.001 kpc	0.001
Pitch angle	p_s	7°33'	0.45
Gap parameters:			
ϕ_1^a		1°500'	...
ϕ_2/ϕ_1		-0.643	0.017
Half width	w_s/ϕ_1	16.28 pc deg ⁻¹	0.70
Height	Z_s/ϕ_1	11.9 pc deg ⁻¹	2.9
Central density	ρ_s	156 MJy sr ⁻¹ kpc ⁻¹	29
Emissivities	k_+/k_-	3.09	0.52
Spiral arms:			
Emissivity ^a	k_a	1.00	...
Density	ρ_a	162 MJy sr ⁻¹ kpc ⁻¹	28
Cut-off radius	r_m	6.71 kpc	0.48
Cut-off scale length	r_a	2.07 kpc	0.22
Arm width coefficient	c_a	64.1 pc kpc ⁻¹	8.8
Initial scale height ^a	$h_{0,a}$	80.0 pc	...
Flair radius	$r_{f,a}$	5.48 kpc	0.13
Fflair coefficient	$h_{1,a}$	14.6 pc kpc ⁻²	1.4
Sag-Car reduction factor	f_r	0.407	0.036
Warp:			
Radius that warp starts	R_w	6.993 kpc	0.046
Phase of the warp	ϕ_w	-0°12'	0.45
Amplitude coefficient	a_w	72.8 pc kpc ⁻²	7.0

^a Fixed parameters.

the vertical coordinate of the Sun, Z_\odot , and the offsets $Q_{J,K}$. The stellar model possesses only a single parameter that is explicitly fixed, the scale height of the stellar spiral arms, set to be equivalent to that of the dust ($h_a^* = h_{0,a}$). However, several assumptions are made with regard to common geometry between the dust and the stellar distributions, such as the radius that the warp starts.

The parameters resulting from the NIR adjustment are given in Table 2. The NIR sky maps of the DIRBE instrument and of the model are given in Figures 8 and 9, as well as the relative differences between the data and the model, $(D^{\text{obs}} - D^{\text{mod}})/D^{\text{obs}}$. The sky maps of the observations and model look very similar, the deviations being obvious only in the relative difference maps. These show that the largest deviations are in the GP within 30° of the GC. Again, to show in more detail the concordance and deviations between the observed and the modeled emission, especially in and near the GP, emission profiles at various latitudes are shown in Figures 10, 11, and 12.

The observed NIR emission profiles are much smoother than those seen in the FIR, and in contrast to the FIR the axisymmetric component dominates the emission profiles at all latitudes. The profiles deviate most from an ideal axisymmetric profile as one approaches the GP, especially in J , and this is largely due to absorption. The spiral arms are much less evident than in the FIR, and only provisionally identifiable in the K band (Drimmel 2000). Indeed, differentiating between emission and absorption features in the NIR is problematic, and it has been suggested that deviations from axisymmetry in the NIR can be attributed to

absorption effects alone (Kent et al. 1991). The two absorption features most clearly evident are due to the local arm, seen at $l \simeq 80^\circ$ and -100° .

In the modeled emission profiles the effect of using a rescaled dust model to calculate extinction is immediately obvious, introducing fluctuations even on small scales. Incidences can be found where the rescaling introduces spurious features, but more often it allows the model to achieve a correspondence with the data that could not be obtained otherwise. This is particularly evident at low latitudes in J , and shows the importance of absorption at these latitudes in shaping the profiles. Nevertheless, emission from the spiral arms is important in the GP, though we will have to make comparisons with axisymmetric models in § 5 to make this demonstrably obvious.

One nonaxisymmetric feature that is evident in the NIR is the Galactic warp, though less obvious than in the FIR. It reveals itself as an asymmetry in the emission profiles, seen most clearly in Figure 12 at $|b| = 5^\circ$; the profiles are skewed toward positive longitudes at $b = -5^\circ$, and toward negative longitudes at $b = 5^\circ$. This requires a local tilt in the stellar distribution with respect to the $b = 0$ plane, accounted for here by the warp starting within the Solar Circle.

The relative difference map in K suggests the presence of structure not accounted for by the model. Aside from the deviations in the GP mentioned above, broad dark patches in the difference map in K can be seen at positive and negative longitudes. That at positive longitudes, roughly located at $l = 90^\circ$, is distinctly above the GP, and may be

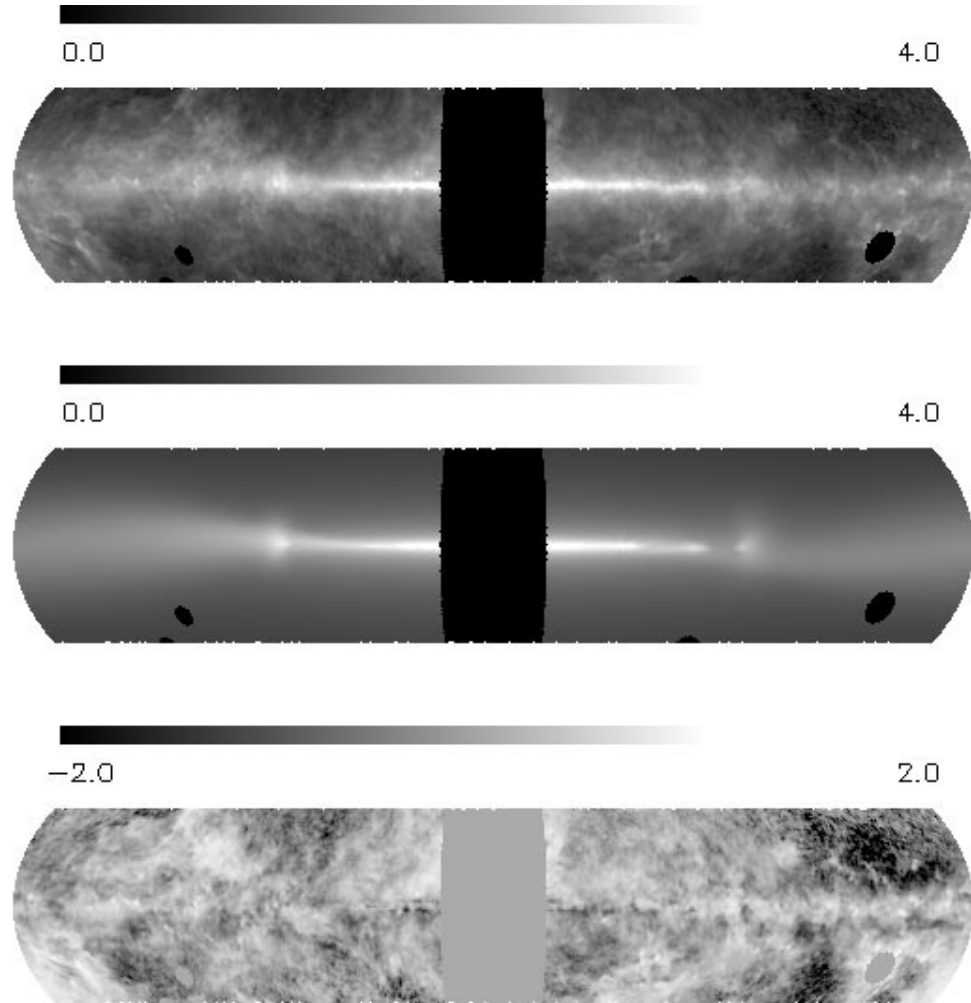


FIG. 4.— $240 \mu\text{m}$ sky maps of the smoothed DIRBE data (top), the modeled emission (middle), and the relative difference between the modeled and observed emission (bottom). The top two maps are on a logarithmic scale, while the bottom map is on a linear scale.

stellar emission associated with the local (Orion) arm. The bright patch at negative longitudes is less obvious, centered on the GP and is found within $l = -90^\circ$, thus not correctly positioned to be associated with the local arm. Additional features seen in the difference map in J are associated with over- or underestimated absorption.

4.3. General Features of the Model

To concisely summarize the general features of the stan-

dard model a “bird’s-eye view” of the Milky Way is presented as a surface density map for the dust in Figure 13, and as a K -band surface brightness map in Figure 14. The center of the maps are determined from an extrapolation of the model, which is itself specifically constructed only for $r > 0.34 R_\odot$, thus the picture presented for $r < 34 R_\odot$ is necessarily incomplete. In particular, no structure associated with the Galactic bulge is represented. Also, the spiral arms are incomplete on the far side of the Galaxy owing to the adopted spiral geometry based on the *observed* $\text{H}\ \text{II}$ regions. The relative strength of the spiral arms in the dust and the stars is shown in Figure 15 as the arm-interarm (flux) density contrast in the GP. However, the difference in the scale heights of the disk and spiral arms mitigate the surface brightness/density contrast between the arm and interarm regions; the arm-interarm ratio in the NIR surface brightness is 1.2 and 1.32 for J and K , respectively. Figure 16 shows the scale heights of the various components.

In addition to the major spiral arms, the dust surface density map shows the smaller local arm in the region of the Sun. Though the local arm produces prominent FIR emission features in our sky, from an extra-Galactic perspective it is revealed to be a minor feature, as pointed out by Georgelin & Georgelin (1976). Indeed, “arm” is perhaps a misnomer. Similar structures are undoubtedly found

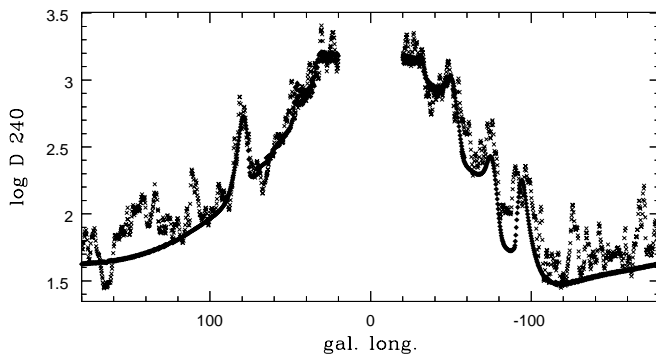


FIG. 5.— $240 \mu\text{m}$ emission profile for the data (crosses) and model (diamonds) within $0^\circ.17$ of the GP ($b = 0$), on a logarithmic scale ($\log D$).

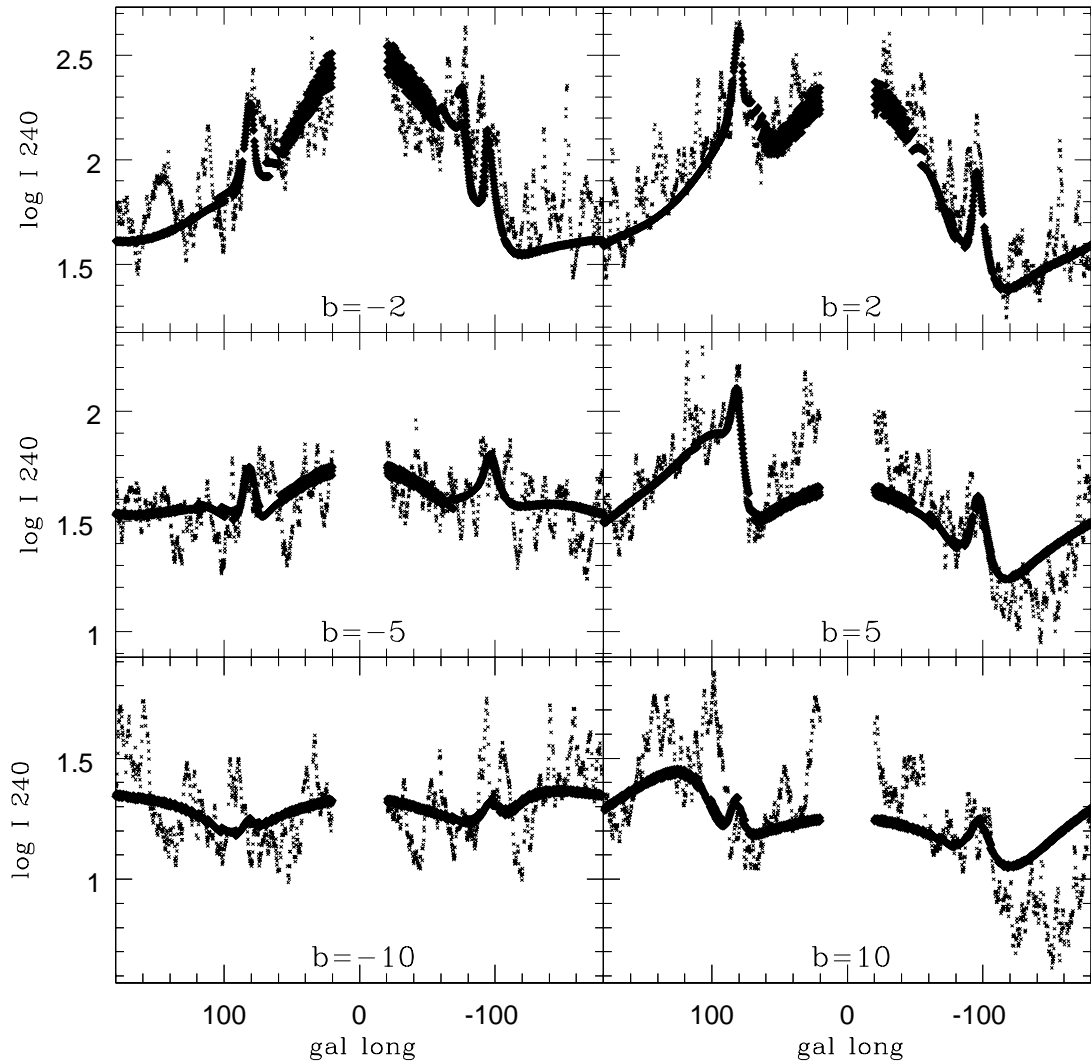


FIG. 6.— $240\text{ }\mu\text{m}$ emission profiles within $0^\circ 17$ of the indicated Galactic latitudes. Scale and symbols are as in previous figure.

throughout the Galaxy in the form of spurs and bridges between the main spiral arms; the local arm is prominent and resolved in our FIR sky only by virtue of its vicinity.

Our flux density model implies an extinction corrected K -magnitude of -23.79 for the Milky Way, assuming $R_\odot = 8$ kpc, of which the spiral arm component contributes 7 percent of the total luminosity. However, our spiral arm model is incomplete for the side of the Galaxy opposite the Sun because of the lack of observed H II regions. Assuming that the spiral arm model is complete over $\frac{3}{4}$ of the Galaxy, the actual contribution of the spiral arms to the total flux would be 10%, resulting in a K -magnitude of -23.82 , which does not include light from the Bulge. The bulge/disk luminosity ratio has been approximately estimated as 0.2 (O. Gerhard 2000, private communication), which results in a final K -magnitude of -24.02 for the Milky Way, consistent with the earlier estimate of Malhotra et al. (1996).

5. UNCERTAINTIES AND ALTERNATIVE MODELS

In this section we explore the sensitivity of the adjusted parameters on the choice of fixed parameters, thereby estimating systematic errors, and test the relative importance of specific features of the model that are not obviously esen-

tial. In particular various spiral models for the stars are considered in an attempt to reproduce the observed NIR emission profiles in the GP.

5.1. Uncertainties

Four of the fixed parameters in the adjustment to the FIR, $(\phi_1, r_f, h_{0,a}, Z_\odot)$, as well as the assumed temperature gradient of the disk component, are each varied in turn from their standard values, and the FIR adjustment redone. The resulting values of the adjusted parameters are shown in Table 3. In all these fits R_s , the radius of the local arm, was adjusted to within 0.1 percent of $1 R_\odot$, and has thus been left out of the table. The resulting χ^2 of these fits fell within 1% of that of the adopted standard model, with the exception of the $\phi_1 = 3^\circ$ and $Z_\odot = 10$ pc models whose χ^2 deviated by less than 3%. The variance of the resulting parameters are used as estimates of the uncertainties given in Table 1.

From Table 3 notable correlations between Z_\odot and adjusted parameters are worth mentioning. The strongest is that between Z_\odot and the linear flare parameter h_1 of the dust disk, and we have excluded these models in the calculation of the uncertainty of h_1 . There are also strong correlations with Q_{240} and the spiral parameters c_a and $h_{1,a}$. For

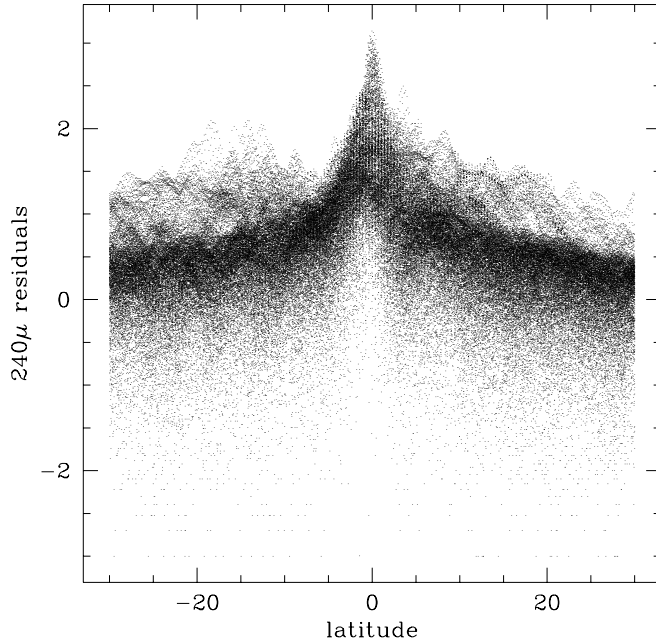


FIG. 7.—Logarithm of the absolute FIR deviations, between the data and the model, as a function of Galactic latitude.

the local arm many of the parameters are correlated to the value of ϕ_1 . In the case of the density and emissivity this is expected, however the initial intention of the “geometrical” parameters ϕ_2/ϕ_1 , w_s/ϕ_1 , and Z_s/ϕ_1 was to allow an eventual adjustment of ϕ_1 alone in the adjustment to the NIR data to arrive at the relative placement of the local arm. If this were possible then these geometrical parameters would

be independent of the choice of the initial ϕ_1 . However, this is not realized. For this reason ϕ_1 is kept fixed in the NIR adjustment.

To estimate the uncertainties in the stellar parameters the 10 parameter sets derived from the FIR adjustments shown in Table 3 were in turn used for a suite of NIR adjustments, allowing an estimate of the uncertainties in the stellar parameters to be made. In contrast to the dust model, the stellar model only has one fixed parameter, the scale height of the stellar spiral arms, and this parameter is effectively varied in this suite of adjustments because $h_a^* = h_{0,a}$. The resulting sets of parameters are shown in Table 4.

Inspection of the disk parameters for the different models shows evidence of clustering about two solutions, probably a result of two minima in χ^2 space, one with an average scale length of 2.56 kpc (three models), and the other with an average scale length 2.19 kpc (for $R_\odot = 8$ kpc). The standard model belongs to the latter group and the uncertainties for the disk parameters given in Table 2 is from the variance of the seven models belonging to this shorter radial scale length solution. The χ^2 only slightly distinguishes between these two solutions, the longer scale length solutions having an average χ^2 2% lower than that of the standard model. The variance from all 10 models is given in parenthesis. The other parameters do not seem to reflect this clustering, with the exception of κ_V . Excluding the three longer scale length models reduces the uncertainty of this parameter to 0.0025. Meanwhile the uncertainties for the dust densities and emissivities are found after excluding the $\phi_1 = 3^\circ$ and $Z_\odot = 10$ pc models, which have spiral arm emissivities that are more than three standard deviations from the mean. Again, the variances from all ten models is given in parenthesis.

TABLE 2
STELLAR PARAMETERS

Parameter	Symbol	Value	Uncertainty
Disk:			
Normalization in J	η_J^0	14.7 MJy sr $^{-1}$ kpc $^{-1}$	2.3 (4.2)
Normalization in K	η_K^0	11.6 MJysr $^{-1}$ kpc $^{-1}$	1.7 (3.2)
Radial scale length	r_*	2.264 kpc	0.083 (0.19)
Scale height	h_*	282.2 pc	7.9 (20.)
Cutoff radius	r_c	10.52 kpc	0.34
Spiral arms:			
Amplitude in J	B_J	0.86	0.25
Amplitude in K	B_K	1.28	0.24
Mean age in J	τ_J	5.5 Myr	3.6
Mean age in K	τ_K	17.6 Myr	3.8
Arm width coefficient	c_J^*	142 pc kpc $^{-1}$	43.
Arm width coefficient	c_K^*	143 pc kpc $^{-1}$	69.
Corotation radius	i	6.66 kpc	0.39
Dust:			
V opacity	κ_V	0.0180 (MJy sr $^{-1}$) $^{-1}$	0.0029
Emissivities	k_+	3.98	0.35 (0.45)
	k_-	1.29	0.10 (0.26)
	k_a	2.07	0.37 (2.9)
Densities	ρ_s	121. MJy sr $^{-1}$ kpc $^{-1}$	23. (32.)
	ρ_a	61. MJy sr $^{-1}$ kpc $^{-1}$	16. (26.)
Miscellaneous:			
Height of Sun	Z_\odot	14.6 pc	2.3
Warp coefficient	a_w	27.4 pc kpc $^{-2}$	2.5
J offset	Q_J	-0.0684 MJy sr $^{-1}$	0.0082
K offset	Q_K	-0.0744 MJy sr $^{-1}$	0.0069

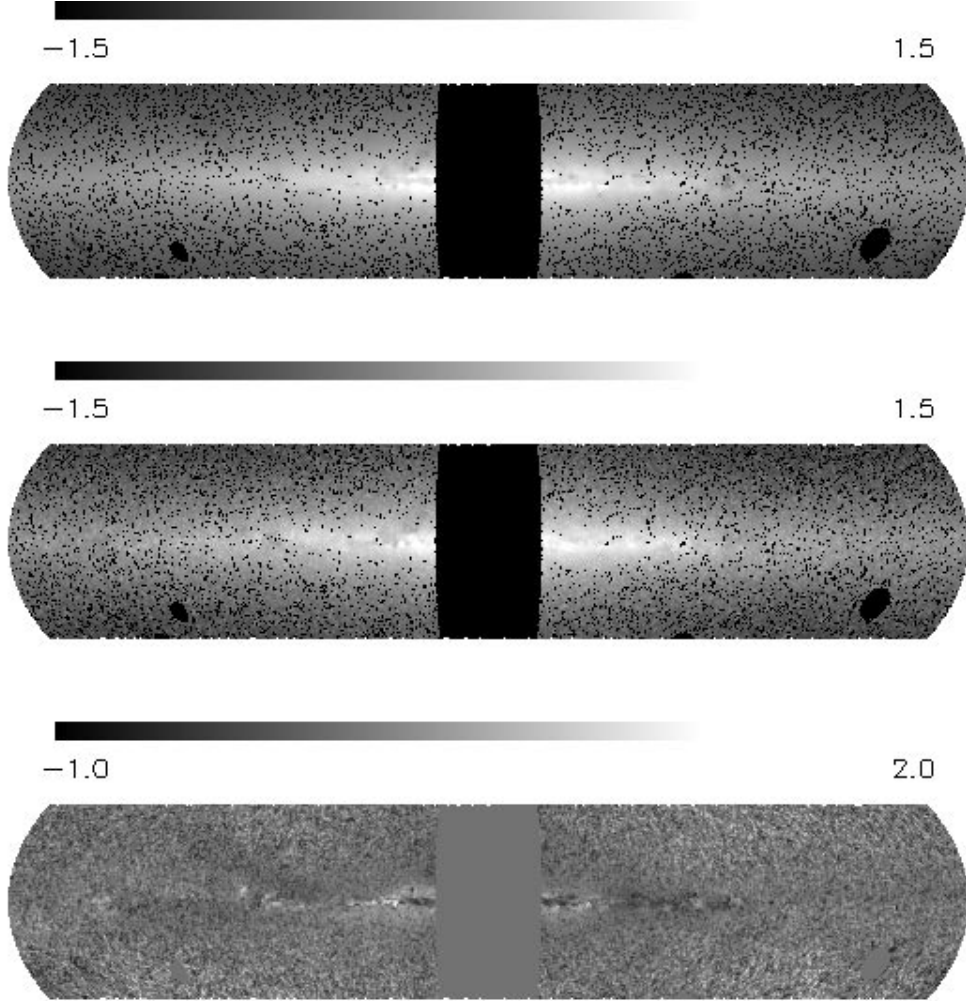


FIG. 8.—Sky maps of the observed J -band emission (top), the predicted J -band emission from the stellar distribution model (middle), and the relative difference map between model and data (bottom). Black pixels in the upper two maps show pixels removed from the data set, due to blanking out selected regions, such as the Galactic center, or rejected point sources. Upper two maps are on a log scale, while the bottom is on a linear scale.

The magnitude of the relative uncertainties are in most cases between 10% and 15%, though are higher for the parameters associated with the spiral arms. The data in or near the GP, where most of the information resides for the spiral arm parameters, makes up a relatively small fraction of the χ^2 , with the result that these parameters are not as well determined. Possibly another choice of merit function more sensitive to the GP emission would render a better determination of these parameters.

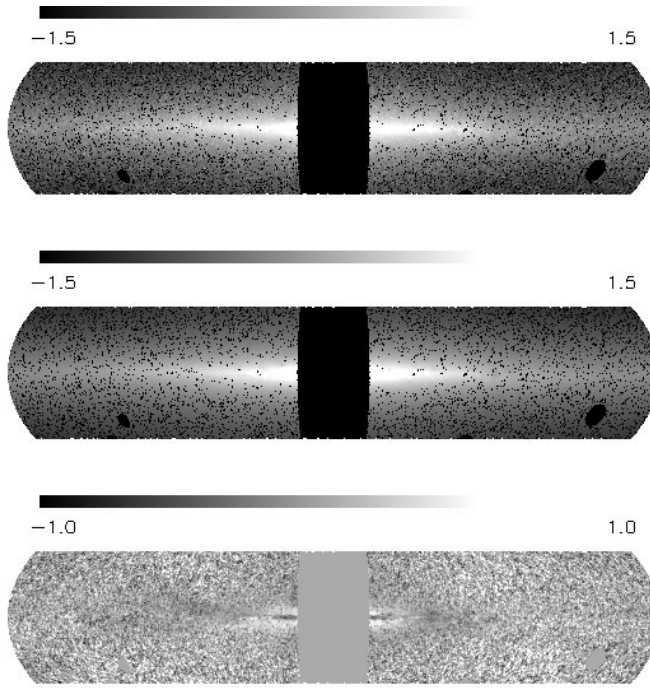
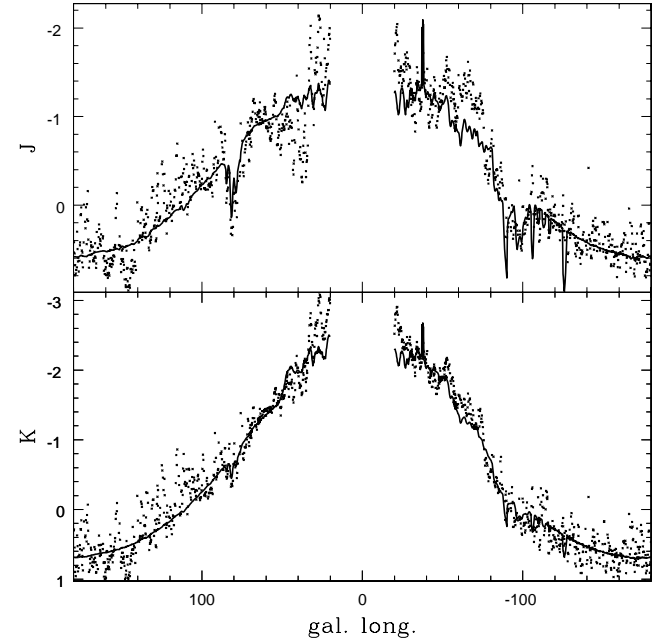
5.2. Alternative Models

Besides the above models we have also run a suite of models to test the sensitivity of our results with respect to the data selection and specific features in the models. Adjustments to data restricted to smaller latitudes ($|b| < 20^\circ$), or with a model lacking a central hole in the dust disk, or with a radial cutoff in the dust disk imposed at $1.75 R_\odot$, each produced estimated parameters that coincided with the standard model well within the given uncertainties. However, the adjustment is sensitive to varying the cut in Galactic longitude, as including emission within 20° of the GC will include emission from structures not

described by the model, such as the Galactic bulge, and excluding emission within 30° of the GC would exclude important arm tangents needed to constrain the spiral arms.

Other alternative stellar models worthy of discussion are given in Table 5. A model with a flair in the stellar disk, starting at the same radius as the flair in the dust disk, was fitted to the data. The resulting flair parameter was quite modest, 6.6 pc kpc^{-1} , less than half that found for the dust disk, but leads to a moderately larger scale height. No significant improvement of the χ^2 is seen ($< 1\%$), thus no positive evidence for such a structure can be inferred. Removing the disk cutoff results in a significant change of only a few parameters, while the χ^2 was only slightly larger than that of the standard model; this is another feature of the stellar disk which is not well constrained. However, the necessity of the NIR offsets is confirmed. In this case χ^2 increases more than 17% when the offsets are set to zero, but most of the parameters are not significantly different than the normative values.

A model in which the dust emissivity of the dust spirals was fixed to unity was adjusted; though this has a signifi-

FIG. 9.—Same as the previous figure, but for the K bandFIG. 10.—Observed (crosses) and modeled (solid line) J - and K -band emission within 0.2 of the GP for the sheared spiral arms model. Vertical scale is in magnitude units ($-2.5 \log D_b$).

cant effect on the amplitude of the stellar spirals, other parameters are not affected, nor is the χ^2 very different from the standard model. This insensitivity shows that the dust density (and emissivity) associated with the spiral arms are

not well constrained, but likewise neither are the other parameters affected by this uncertainty. Another adjustment was done with the scale height of the stellar spirals set to twice that of the dust spirals. This modification significantly

TABLE 3
DUST MODELS WITH VARIABLE CONSTANTS

PARAMETER	UNITS	$h_{0,a}$ (pc)		$r_{f,a}$ (R_\odot)		ϕ_1		Z_\odot (pc)		∇T (K/R_\odot)	
		60	100	0.5	0.6	1°0	3°0	10	20	-5.5	-7.5
Disk:											
ρ_0	MJy sr $^{-1}$ kpc $^{-1}$	1122	1112	1057	1096	1120	1172	1018	1060	1084	1067
h_r	kpc	2.21	2.28	2.26	2.31	2.19	1.93	2.52	1.99	2.22	2.32
$h_{0,d}$	pc	139.0	131.5	132.4	135.9	135.3	157.3	135.0	153.1	136.7	134.5
$h_{1,d}$	pc kpc $^{-1}$	16.5	14.7	15.3	12.3	20.9	44.1	0.8	46.4	13.5	14.5
Q_{240}	MJy sr $^{-1}$	1.04	1.16	1.07	1.13	1.00	0.97	1.42	0.82	1.10	1.09
Local Arm:											
p_s	deg	7.35	7.36	6.88	7.38	7.96	6.37	7.74	7.88	7.17	7.21
ϕ_2/ϕ_1		-0.648	-0.635	-0.634	-0.660	-0.654	-0.640	-0.666	-0.619	-0.680	-0.657
w_s/ϕ_1	pc deg $^{-1}$	16.43	16.25	16.65	16.21	16.88	18.46	15.85	17.08	17.09	16.50
Z_s/ϕ_1	pc deg $^{-1}$	12.0	12.1	11.8	11.9	17.5	5.7	9.5	14.7	11.8	11.8
ρ_s	MJy sr $^{-1}$ kpc $^{-1}$	161	158	160	155	223	101	152	183	152	158
k_+/k_-		2.84	2.82	2.71	3.15	2.90	1.47	3.31	2.09	2.76	2.86
Spiral arms:											
ρ_a	MJy sr $^{-1}$ kpc $^{-1}$	174	130	165	160	148	87	139	104	164	162
r_m	kpc	6.36	7.45	6.56	6.77	7.16	7.85	7.19	7.53	6.55	6.73
r_a	kpc	2.23	1.68	2.15	2.02	1.81	1.59	1.78	1.74	2.14	2.05
c_a	pc kpc $^{-1}$	69.6	57.4	66.3	60.7	67.6	81.4	53.1	81.5	64.9	64.1
$r_{f,a}$	kpc	5.38	5.71	5.45	5.46	5.69	5.38	5.32	5.34	5.42	5.48
$h_{1,a}$	pc kpc $^{-2}$	14.7	14.5	14.2	14.9	14.6	11.3	15.3	11.0	14.2	14.5
f_r		0.432	0.384	0.406	0.404	0.409	0.518	0.420	0.440	0.404	0.406
Warp:											
R_w	kpc	7.016	6.973	6.990	7.000	7.017	7.053	7.132	7.041	6.966	6.996
ϕ_w	deg	0.18	0.05	0.02	-0.30	0.43	1.28	0.44	0.57	-0.14	-0.11
a_w	pc kpc $^{-2}$	75.9	73.6	72.7	73.8	77.5	86.7	91.8	84.4	70.3	73.4

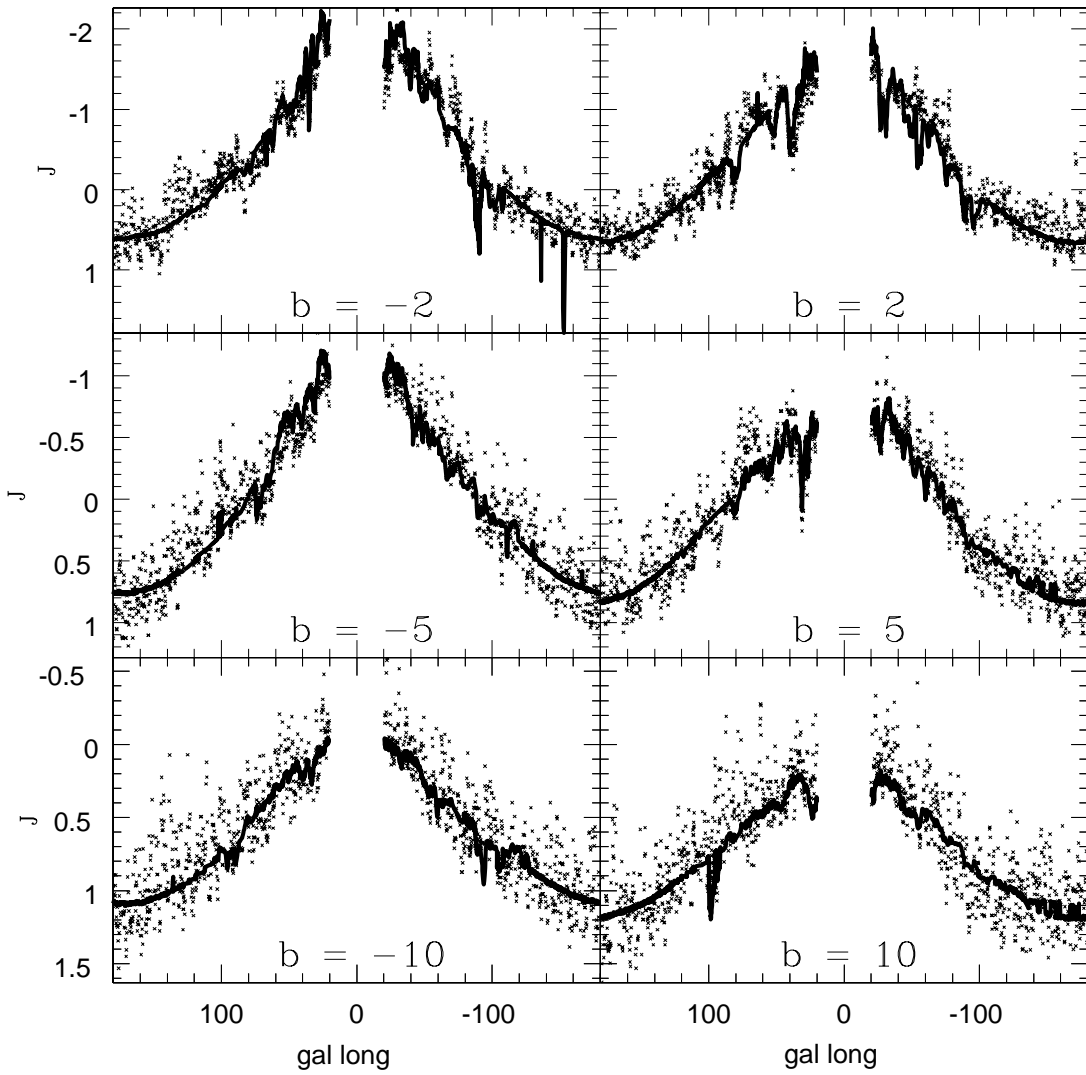


FIG. 11.— J -band emission as observed and modeled within $0^{\circ}2$ of the indicated latitudes. Scale, symbols, and units are as in previous figure.

changes some of the parameters, including the disk scale length, but is not favored as the total χ^2 is 3% higher than for the standard value. This and other experiments confirm that a small scale height is favored for the stellar spirals.

In order to discern the nonaxisymmetric structure in the Galactic disk from the NIR emission, four different models were adjusted against the data, three spiral models and a purely axisymmetric model. Figures 17 and 18 show the GP emission profiles for longitudes $|l| < 90^\circ$ of the four models, and Table 6 gives their parameters and χ^2 in the GP. The two logarithmic spiral models use a single amplitude parameter B for both wavebands, consistent with the hypothesis that the spiral structure has the same stellar population as the disk. Meanwhile the sheared spiral model is formulated under the assumption that they primarily consist of young stars born from the spiral arms traced by the dust, and are thus given parameters that differ from one waveband to the other. As can be seen in Figures 17 and 18, the $m = 2$ log spiral model and the sheared spiral model perform about equally well, while the nonaxisymmetric and $m = 4$ models fail to produce emission apparently associated with the spiral arms, particularly in the directions to the tangents of the Scutum arm, $l \approx 30$ and -50° .

At positive longitudes no clear evidence of the Sag-Car arm is present; the axisymmetric and $m = 2$ log spiral models reproduce the emission profile at $l > 40^\circ$ as well as the other two spiral models, though the former two models do not possess the Sag-Car spiral arm. However, a closer comparison of the $m = 2$ log and sheared spiral models suggest that the Sag-Car arm is indeed present, at least at negative Galactic longitudes; the parameters common to the $m = 2$ log and sheared spiral model are similar, though the very large pitch angle of the $m = 2$ log spiral produces a geometry significantly different from that of the sheared spiral model (see Fig. 19). This high estimate of the pitch angle is most likely due to an effort in the model to account for emission at longitudes $l < -50^\circ$, which is more prominent in J . Indeed, adjustment of an $m = 2$ log spiral model to the K -band alone gives a smaller estimate of the pitch angle of 15.6 (Drimmel & Spergel 2001). All four of the models are inadequate in reproducing emission for $|l| < 30^\circ$.

In fitting the four above models to the NIR data it was necessary to fix the emissivity of the spiral arms in the dust for the axisymmetric case. Decoupling of the emissivity and density of the dust spiral component was successful for the

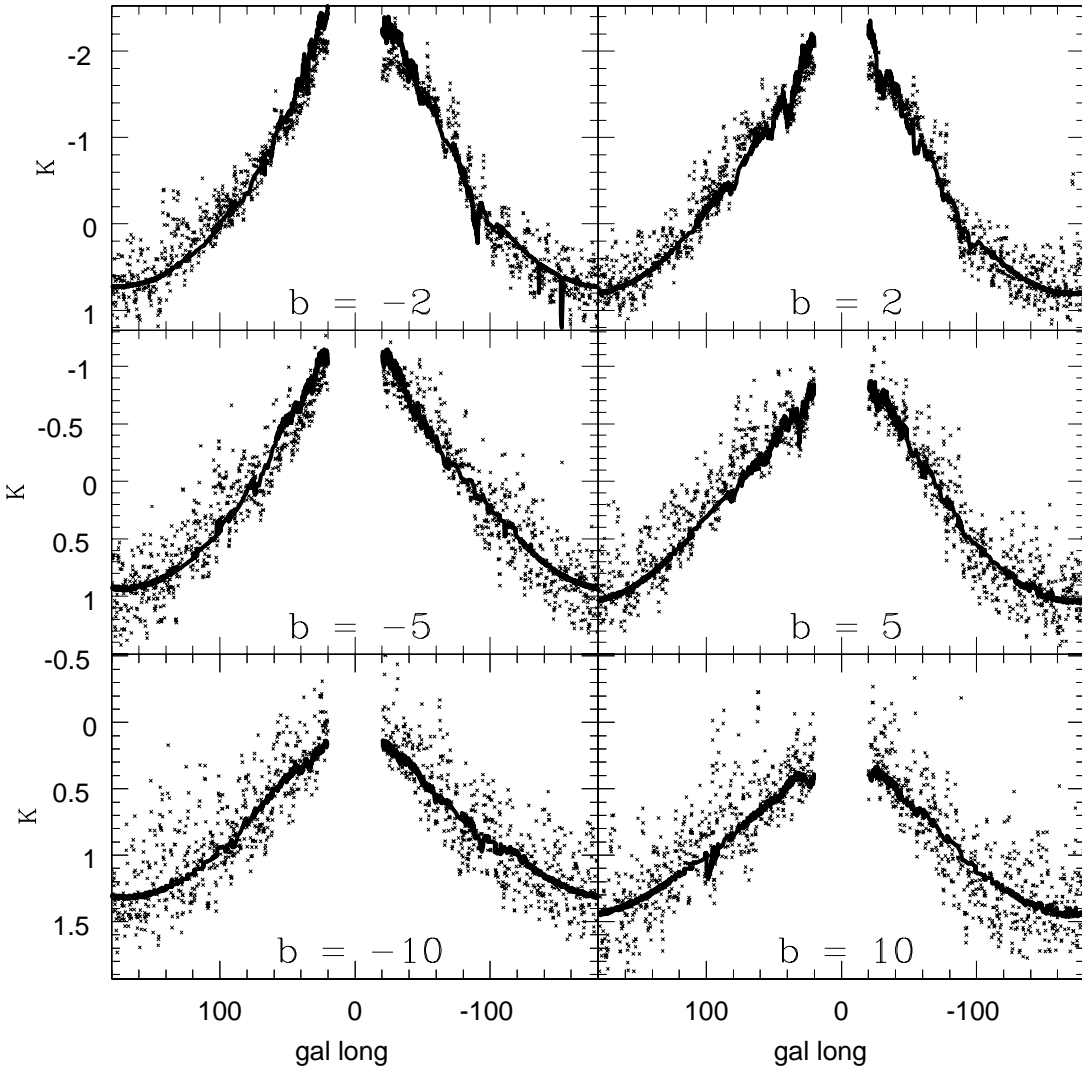


FIG. 12.—K-band emission as observed and modeled within $0^{\circ}2$ of the indicated latitudes. Scale, symbols, and units are as in previous figure.

other three models, though questionably reliable for the $m = 4$ model that gave an emissivity much higher than the disk component.

6. DISCUSSION

6.1. Axisymmetric Structure

The scale length of the axisymmetric component of the dust distribution is here found to be $0.28 R_{\odot}$, which is shorter than that of F98 ($0.37 R_{\odot}$), and significantly shorter than that of either Spergel et al. (1996) ($0.48 R_{\odot}$) or Davies et al. (1997) ($0.62 R_{\odot}$). Apparently a more extended dust component is not needed when the distribution of the warmer (nonaxisymmetric) components are taken into account. Other models of the Galactic dust distribution are based on correlating the dust density with the gas (hydrogen) surface density (e.g. Ortiz & Lepine 1993). Such models point out that an exponential disk model is not appropriate in the central regions of the Galaxy ($r < 0.5 R_{\odot}$), where the gas surface density shows a hole. Nevertheless, a characteristic scale length can be assigned to the outer regions, and these show a much wider range than those stated above due to uncertainties in the metallicity gradient and the CO:H₂ ratio. The latter is usually taken as

constant with Galactocentric radius, but recently it has been argued that this ratio may vary considerably with Galactocentric radius (Sodroski et al. 1997).

A feature seen in the H I distribution that we have included in our model is a flair in the disk scale height. Malhotra (1995), using a Gaussian vertical density profile for the H I, finds a scale height that flares from ~ 100 pc to ~ 220 pc going from 0.5 to $1.0 R_{\odot}$. (Here and in what follows, quantities expressed in parsecs are derived on the assumption that $R_{\odot} = 8$ kpc.) We find a smaller initial scale height and more modest gradient, the scale height increasing from 134 to 188 pc at the Solar Circle. These values are comparable to the constant scale height of F98 (152 pc), but smaller than the much higher value of 470 pc of Davies et al. (1997). A possible source of bias in our determination of the dust scale height is the assumption of no vertical temperature gradient, which if present would result in the scale height of the dust being underestimated. However, we expect the vertical temperature gradient to be small for the dust disk component, as the scale height of the stars heating the dust is significantly larger than that of the dust.

The isotropic offset parameter Q_{240} corresponds to the CIB. Our value for the CIB, 1.07 ± 0.15 MJy sr⁻¹, is in agreement with other determinations (1.17 ± 0.53 MJy sr⁻¹

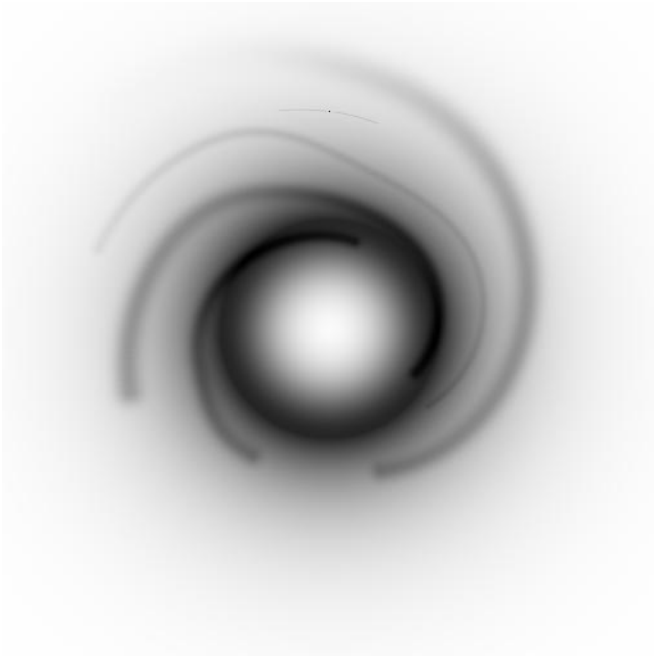


FIG. 13.—Surface density map of the dust, as inferred from the dust density model. Small black dot (*upper center*) shows the position of the Sun, which nearly lies on a small local feature, known as the Orion arm. Arms are incomplete on the side opposite the Sun owing to incomplete H II data.

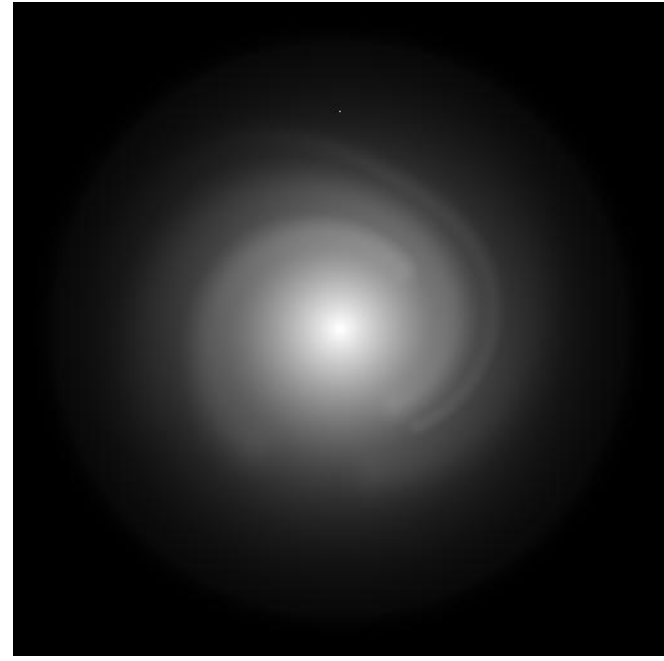


FIG. 14.—Surface brightness map of the Milky Way in the K -band. Bright dot (*upper center*) indicates the position of the Sun.

TABLE 4
STELLAR MODELS WITH VARIABLE CONTENTS

PARAMETER	UNITS	$h_{0,a}$ (pc)		$r_{f,a}$ (R_\odot)		ϕ_1		Z_\odot (pc)		∇T (K/ R_\odot)	
		60	100	0.5	0.6	1°0	3°0	10	20	-5.5	-7.5
Disk:											
η_J^0	MJy sr $^{-1}$ kpc $^{-1}$	18.6	7.6	14.6	20.5	8.6	15.6	14.7	16.3	14.6	9.4
η_K^0	MJy sr $^{-1}$ kpc $^{-1}$	14.7	6.2	11.5	15.8	6.9	12.4	11.5	13.1	11.6	7.5
r_*	kpc	2.063	2.596	2.264	2.101	2.564	2.220	2.264	2.186	2.264	2.514
h_*	pc	290.5	329.5	283.3	265.1	318.0	283.6	279.3	284.7	283.2	309.4
r_c	kpc	11.48	10.66	10.55	10.45	10.58	10.17	10.36	10.51	10.59	10.56
Spiral arms:											
B_J		1.50	0.89	0.85	0.76	0.94	0.66	0.88	0.58	0.82	1.01
B_K		1.24	1.43	1.30	1.07	1.62	1.04	1.15	1.76	1.29	1.49
τ_J	Myr	12.7	11.4	9.0	7.1	7.4	16.3	12.5	9.2	3.7	7.3
τ_K	Myr	24.5	13.7	17.2	23.2	13.7	20.4	19.0	17.9	14.9	15.4
c_J^*	pc kpc $^{-1}$	158.	198.	135.	143.	145.	79.	208.	72.	132.	158.
c_K^*	pc kpc $^{-1}$	310.	193.	139.	153.	136.	100.	206.	54.	134.	165.
R_C	kpc	5.67	6.81	6.69	6.12	6.72	6.44	6.33	6.86	6.95	6.62
Dust:											
k_+		4.16	3.46	3.64	4.36	3.53	2.64	3.94	4.03	3.62	3.42
k_-		1.46	1.23	1.34	1.38	1.22	1.80	1.19	1.93	1.31	1.19
k_a		1.77	2.46	2.80	2.37	2.94	10.65	2.65	7.99	2.84	2.56
ρ_s	MJy sr $^{-1}$ kpc $^{-1}$	110.	128.	119.	112.	183.	56.	128.	95.	116.	132.
ρ_a	MJy sr $^{-1}$ kpc $^{-1}$	98.	53.	59.	68.	50.	8.	53.	13.	58.	63.
Misc.:											
κ_V	(MJy sr $^{-1}$) $^{-1}$	0.0177	0.0149	0.0182	0.0194	0.0152	0.0235	0.0170	0.0225	0.0182	0.0155
Q_J	MJy sr $^{-1}$	-0.0441	-0.0704	-0.0682	-0.0680	-0.0691	-0.0672	-0.0715	-0.0608	-0.0673	-0.0711
Q_K	MJy sr $^{-1}$	-0.0565	-0.0781	-0.0743	-0.0715	-0.0791	-0.0737	-0.0762	-0.0669	-0.0738	-0.0790
Z_\odot	pc	14.9	14.4	14.8	14.9	14.8	14.8	10.0	19.8	14.8	14.5
a_w	pc kpc $^{-2}$	25.0	25.4	26.9	29.8	26.1	27.6	33.3	26.5	26.2	26.5

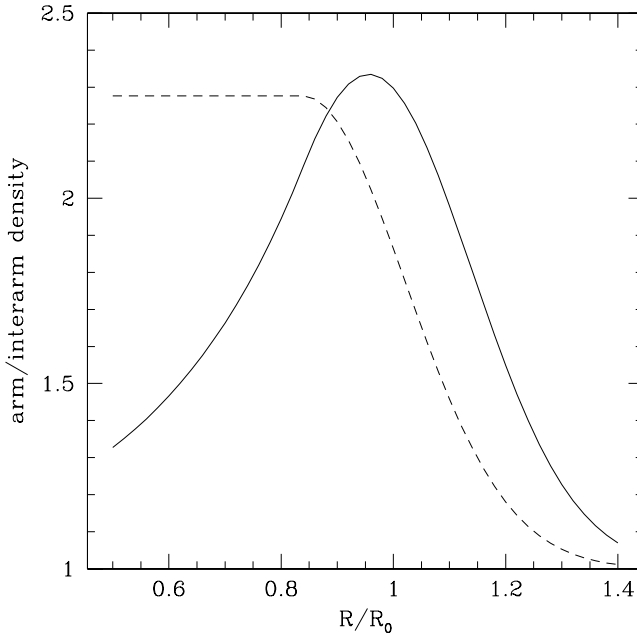


FIG. 15.—Arm-interarm density ratio for the stellar (dashed curve) and the dust spiral arms (solid curve).

[Finkbeiner et al. 2000]; 0.91 ± 0.15 MJy sr $^{-1}$ [Lagache et al. 1999]; 1.09 ± 0.20 MJy sr $^{-1}$ [Hauser et al. 1998]). All estimates agree when an additional systematic error of ± 0.20 MJy sr $^{-1}$ is taken into account.

Our estimate of the stellar radial scale length of the Galactic disk ($0.28 R_\odot$) is shorter than older determinations from NIR data ($0.38 R_\odot$; Kent, Dame, & Fazio 1991). We discuss the implications of this result in the conclusions.

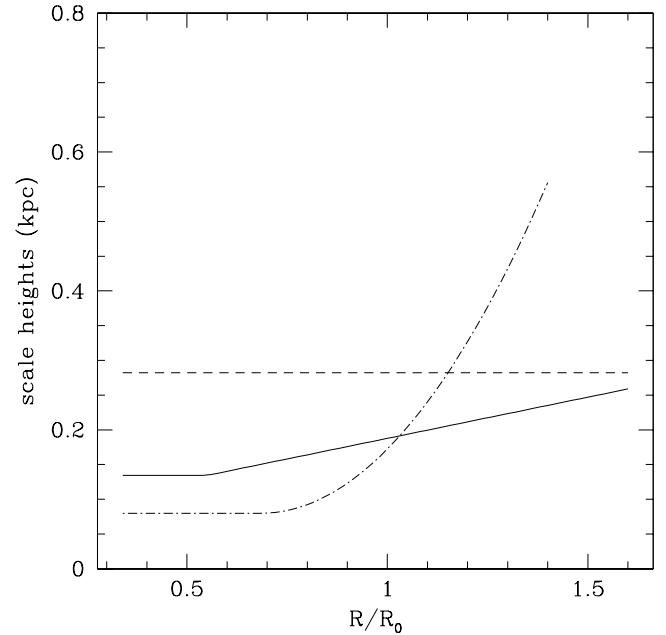


FIG. 16.—Scale heights as a function of radius for the stellar disk (dashed line), the dust disk (solid line), and spiral arms (dot-dashed line), assuming $R_\odot = 8$ kpc.

Our determination of the stellar and dust scale lengths are most sensitive to their distribution between 0.5 and $1 R_\odot$. Our model is not sensitive to a cutoff in the dust density, though we do find a cutoff in the stellar light distribution at approximately 10.5 kpc, which is comparable though smaller than that found by (Ruphy et al. 1996) from a star count analysis of DENIS data. However, it is still larger

TABLE 5
ALTERNATIVE STELLAR MODELS

Parameter	Units	stellar flair	$r_c = \infty$	$Q_{J,K} = 0$	$k_a = 1$	$h_a^* = 2h_{0,a}$
Disk:						
η_J^0	MJy sr $^{-1}$ kpc $^{-1}$	12.2	13.2	10.2	14.1	22.8
η_K^0	MJy sr $^{-1}$ kpc $^{-1}$	9.7	10.3	7.4	11.1	16.9
r_*	kpc	2.319	2.255	2.302	2.273	2.06
h_*	pc	292.3	309.0	306.30	285.6	253.2
r_c	kpc	11.10	∞	12.41	10.54	10.90
Spiral arms:						
B_J		1.06	0.97	0.69	1.33	0.14
B_K		1.62	1.24	1.40	1.64	0.44
τ_J	Myr	4.0	-13.2	17.5	7.5	15.6
τ_K	Myr	11.8	13.3	27.6	14.3	26.0
c_J^*	pc kpc $^{-1}$	155.	266.	136.	173.	95.
c_K^*	pc kpc $^{-1}$	151.	262.	413.	164.	328.
R_C	kpc	6.34	6.95	5.96	6.85	6.44
Dust:						
κ_V	(MJy sr $^{-1}$) $^{-1}$	0.0162	0.0178	0.0116	0.0180	0.0188
k_+		3.95	4.17	4.06	4.02	3.38
k_-		1.28	1.35	1.31	1.30	1.09
k_a		2.17	2.08	2.06	1.00	1.59
ρ_s	MJy sr $^{-1}$ kpc $^{-1}$	122.	115.	118.	119.	142.
ρ_a	MJy sr $^{-1}$ kpc $^{-1}$	75.	78.	79.	162.	102.
Miscellaneous:						
Z_\odot	pc	14.8	13.2	14.8	14.7	14.5
a_w	pc kpc $^{-2}$	24.5	19.4	22.0	29.1	25.6
i	MJy/sr	-0.0731	-0.0585	0.0000	-0.0687	-0.0621
Q_K	MJy/sr	-0.0798	-0.0648	0.0000	-0.0740	-0.0620

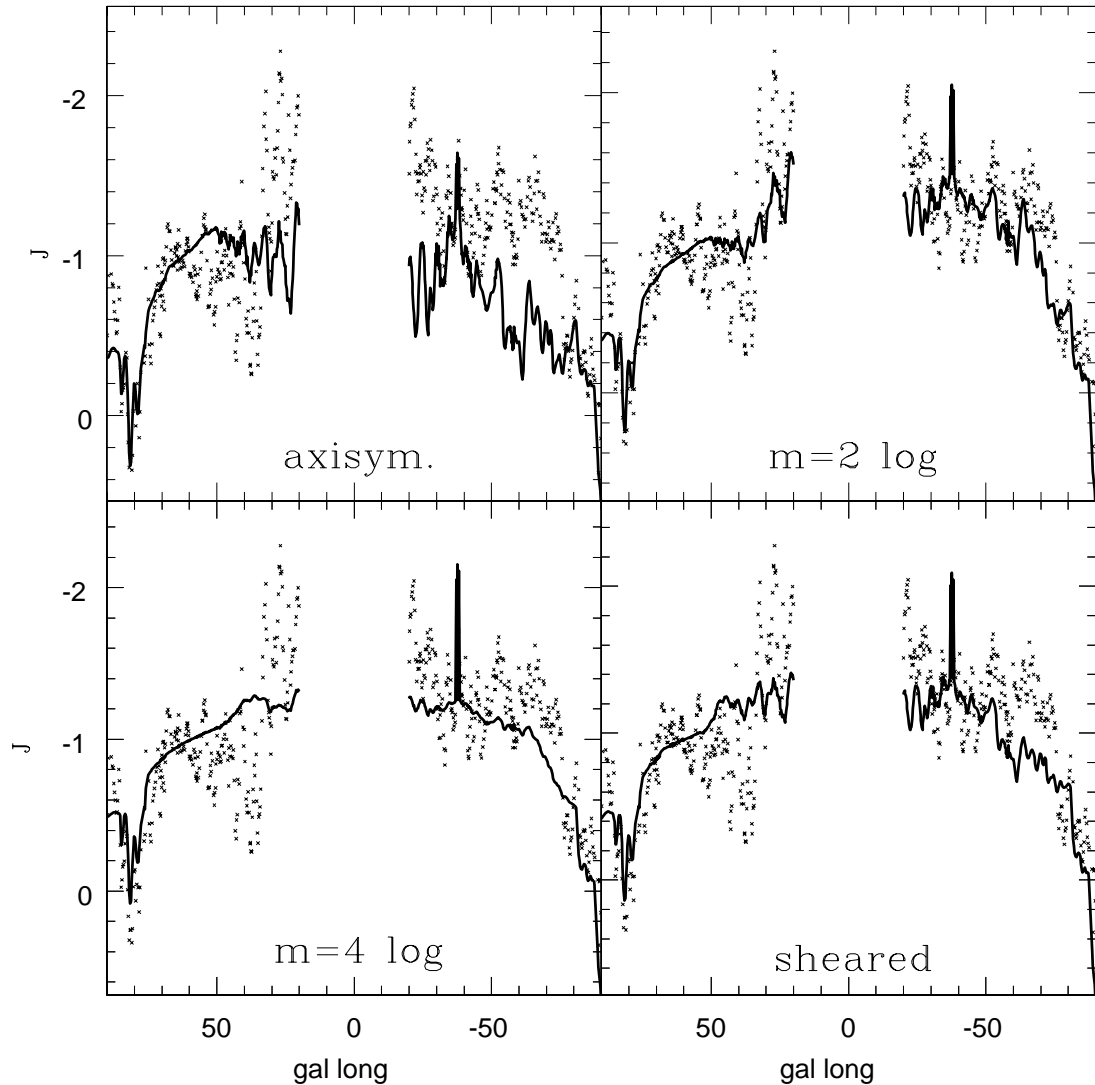


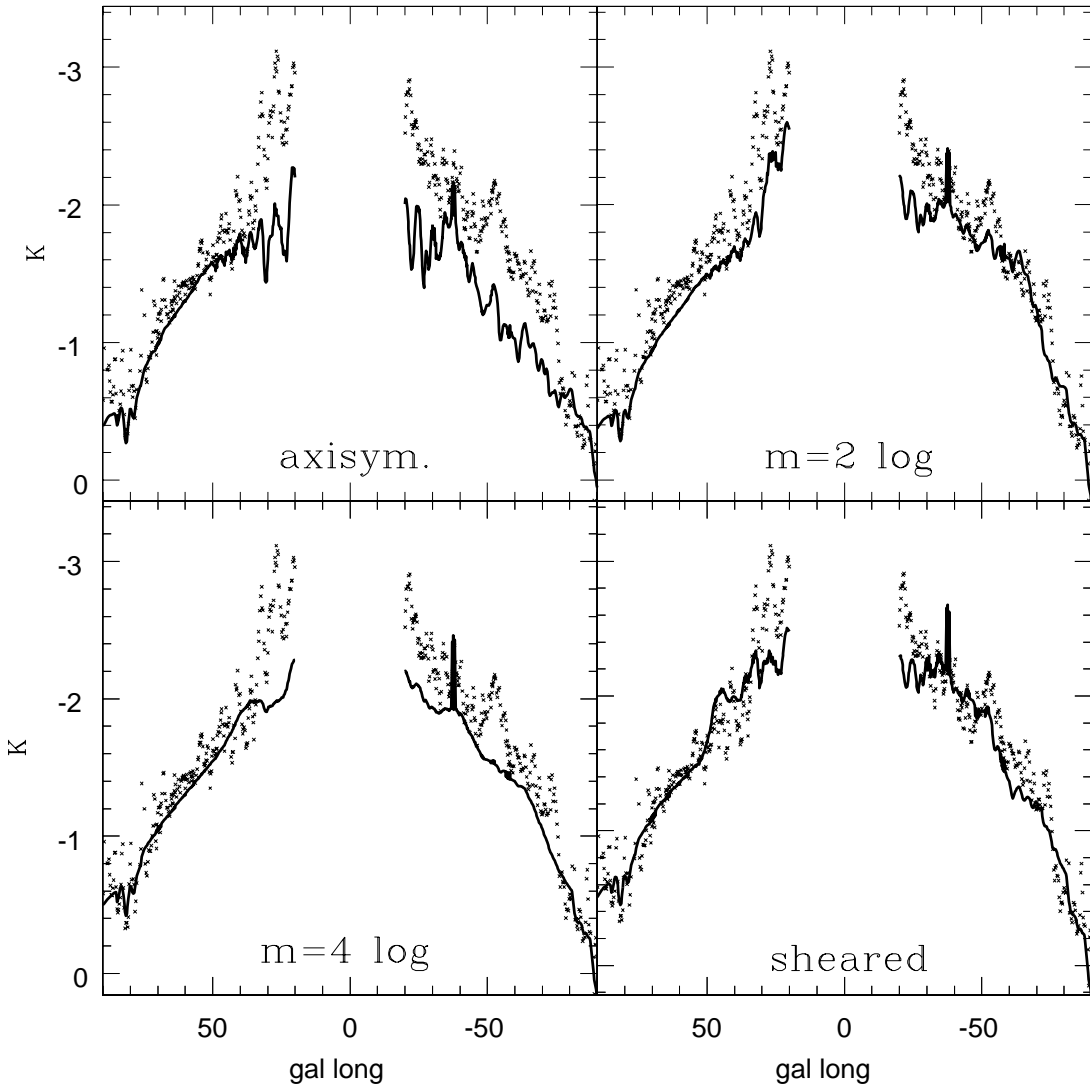
FIG. 17.—Predicted J -band GP emission profiles at $|l| < 90^\circ$ for an axisymmetric model and three spiral models, $m = 2$ and $m = 4$ logarithmic spiral models, and a sheared H II spiral model, plotted against the data (crosses).

than would be expected from the scale length, as compared to external disk galaxies (Pohlen, Dettmar, & Lüticke 2000).

Traditional estimates of scale heights for Galactic stellar populations varies from approximately 90 to 390 pc and are commonly correlated with absolute magnitudes, stellar type, or age in stellar distribution models built to reproduce star count data (Bahcall & Soneira 1980; Ortiz & Lepine 1993; Haywood et al. 1997a). Meanwhile, luminosity density models that reproduce NIR emission on the sky, like our own presented here, have reported scale heights of 247 pc (Kent et al. 1991), 276 pc (Spergel et al. 1996), and 334 pc (F98). Our estimate of 282 pc for the scale height falls among these values. However, scale height estimates do not lend themselves to direct comparison as scale lengths do, because the formulation of the vertical density profile does not enjoy a universal consensus as does the radial profile. In the past vertical exponential profiles were most common, even after it was shown that a sech^2 variation describes an isothermal population in the infinite plane approximation. Recently this situation has changed with more sophisticated models that employ dynamical constraints that have called

into question the traditional exponential vertical profiles (Haywood et al. 1997a; Haywood et al. 1997b). Such models do not possess a simple vertical profile, but only approach an exponential far from the GP, similar to a sech^2 profile. However, this common behavior among the various proposed profiles does not assist us in making comparisons via asymptotic scale heights, as the integrated luminosity is mainly determined by the density variation near the GP.

We note at this point in the discussion two possible sources of biases in our determination of scale heights. The first is the assumption of a constant dust temperature with respect to z and its possible affect on the estimation of the dust scale height, mentioned above, which if present would cause an underestimation of the stellar scale height. The other source of potential bias is the removal of luminosity from point source removal, which preferentially takes place at higher Galactic latitudes where the median background light from unresolved stars is lower. This effect could lead to an underestimate of the vertical scale height. The isotropic term in the emission model may correct for this to some degree, but in the future it will be desirable to make a more accurate correction for this effect.

FIG. 18.—Same as previous figure, but for the K band

6.2. Nonaxisymmetric Structure

Similar to the results of Freudenreich (Freudenreich 1996; Freudenreich 1998) we find a warp that starts within the Solar Circle with larger amplitudes in the dust than in the stars. At $r = 10$ kpc our stellar warp has an amplitude of 0.25 kpc ($R_\odot = 8$ kpc), while F98 finds 0.18 kpc (his model S). From FIR emission we find a dust warp 2.7 times larger, whereas F98 finds an amplitude that is 1.8 times larger as inferred from NIR dust absorption; his dust warp amplitude agrees well with the estimated amplitude of 0.3 to 0.4 kpc that has been given for the warp in H I (Burton & Hartmann 1994). Our warp amplitude in the dust does agree, however, with the warp inferred from the OB stellar distribution (Smart et al. 1998). In the NIR the most important effect of a warp that starts within the Solar Circle is to induce a local tilt ($\tan \theta = h_w(R_\odot)/R_\odot$), as evidenced in the NIR emission profiles at low Galactic latitudes (§ 4.2). For the stars we find a local tilt of $\theta = 0^\circ.2$, while Freudenreich's warp renders a local tilt of $\theta = 0^\circ.5$. A tilt of the stellar distribution with respect to the conventionally defined $b = 0$ plane has also been noted in NIR data by Hammersley et al. (1995), though they propose that a global tilt of the entire stellar disk with respect to the $b = 0$ plane is

responsible for this feature. The motivation for this alternative model is that radio observations seem to indicate the Galactic warp starts beyond the Solar Circle, though this is not well constrained by the radio data. Evidence for a warp being present in the stellar disk is also found in local stellar kinematics, as seen in *Hipparcos* data, though it is more consistent with a warp starting at or beyond the Solar Circle (Dehnen 1998). While the warp both here and in F98 starts within the Solar Circle, this is not a commonly accepted feature of the warp. In any case our warp starts at a significantly larger Galactocentric radius ($\sim 0.85 R_\odot$) than that of F98 (between 0.5 and 0.56 R_\odot), though this difference may only be a consequence of the different functions used to describe the warp amplitude.

With regard to the spiral arms, it was found that an adopted map of H II regions was sufficient to describe the location of peaks in the FIR emission features associated with the spiral arm tangents, though it was necessary to introduce a reduction factor on the Sag-Car arm. This assumed geometry for the spiral arms is consistent with a four arm model of the Galaxy, with a pitch angle of approximately $12^\circ.5$, consistent with other spiral tracers, radio and pulsar data (Vallee 1995). We point out that the dust density

TABLE 6
ALTERNATIVE SPIRAL MODELS

Parameter	Units	Axisymmetric	$m = 2 \log$	$m = 4 \log$	Sheared
Disk:					
η_J^0	$\text{MJy sr}^{-1} \text{kpc}^{-1}$	14.9	15.1	11.8	14.7
η_K^0	$\text{MJy sr}^{-1} \text{kpc}^{-1}$	12.6	12.5	9.9	11.6
r_*	kpc	2.257	2.255	2.386	2.264
h_*	pc	266.8	274.1	286.0	282.2
r_c	kpc	10.70	10.90	10.03	10.52
Spiral arms:					
sheared:					
B_J		0.86
B_K		1.28
τ_J	Myr	5.5
τ_K	Myr	17.6
c_J^*	pc kpc^{-1}	142.
c_K^*	pc kpc^{-1}	143.
R_C	kpc	6.66
logarithmic:					
B		...	1.38	0.42	...
p	deg	...	25.4	15.8	...
R_0	kpc	...	5.38	2.56	...
c_a^*	pc kpc^{-1}	...	138.	99.	...
Dust:					
k_+		2.65	3.61	3.53	3.98
k_-		0.86	1.17	1.14	1.29
k_a		1.00	2.19	11.25	2.64
ρ_s	$\text{MJy sr}^{-1} \text{kpc}^{-1}$	181.	133.	136.	121.
ρ_a	$\text{MJy sr}^{-1} \text{kpc}^{-1}$	162.	74.	14.	61.
Miscellaneous:					
κ_V	$(\text{MJy sr}^{-1})^{-1}$	0.0143	0.0172	0.0158	0.0180
Q_J	MJy sr^{-1}	-0.0533	-0.0633	-0.0640	-0.0684
Q_K	MJy sr^{-1}	-0.0744	-0.0760	-0.0814	-0.0744
Z_\odot	pc	14.7	14.8	14.9	14.6
a_w	pc kpc^{-2}	25.3	24.0	28.4	27.4
χ^2 for $ b < 3^\circ$		65502	51547	53047	51452

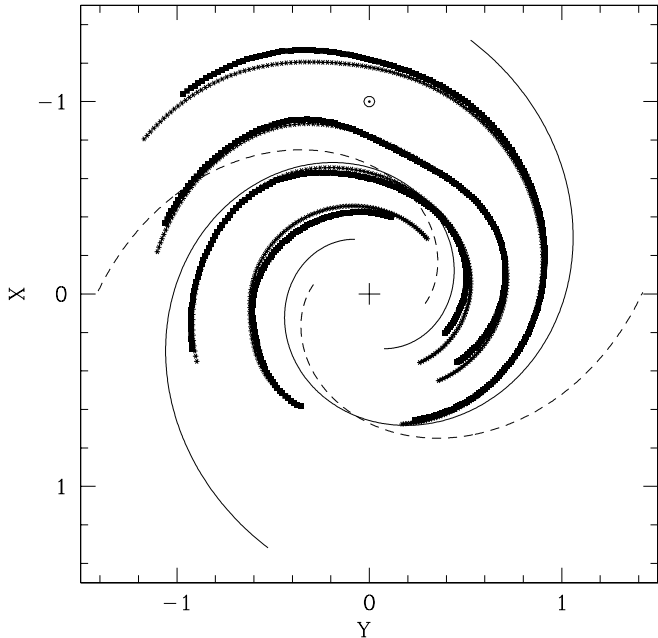


FIG. 19.—Schematic of the Galaxy showing the four spiral arms as mapped by H II regions and the dust (bold lines), the sheared arms in the K band (stars), and the arms in the two-arm logarithmic model for J- and K-band fit (dashed) and the K-band fit alone (solid) (Drimmel, & Spergel 2001). The H II spirals are incomplete on the opposite side of the Galaxy owing to lack of data.

associated with the arms is not well constrained, as strong absorption features from the spiral arms are not present in the NIR to assist in the decomposition of the FIR flux density. Furthermore, there may be significant temperature gradients associated with the arms as the dust here may be primarily heated by young OB stars. By using a single emissivity the widths and scale heights of this component may be significantly underestimated. However, for the same reason that the dust density in the arms are not well determined, this uncertainty does not strongly affect the estimation of the stellar distribution parameters.

Evidence for the spiral structure in the NIR is less evident owing to extinction, but important in and near the GP. Three different geometries were attempted, the geometrical parameters of each model being constrained with the NIR data. Our standard model is a sheared version of the same four arm spiral model used for the dust. Spiral models constructed to describe the distribution of NIR point sources have also utilized four arm models, though of a logarithmic form (Wainscoat et al. 1992; Ortiz & Lepine 1993). One important difference between the spiral model presented here and these previous models is the reduction factor on the size of the Sag-Car arm. The necessity of such a reduction factor is demonstrated by the failure of the $m = 4$ logarithmic model in which all four arms are treated equally, and its effect is consistent with the conclusion that two arms dominate in the NIR. This interpretation is

further supported by the comparable success of a purely two arm spiral model.

We find that the spirals are stronger in K than in J , which also agrees with observations of other spiral galaxies in these wavebands (Grauer & Rieke 1998). The amplitude of our spirals, however, are smaller than those seen in most spiral galaxies; Rix & Zaritsky (1995) report fractional azimuthal variations in the K surface brightness, $(\Sigma_{\max} - \Sigma_{\min})/\Sigma_{\min}$, to be of the order unity for their sample of spiral galaxies, while we find here that this quantity is equal to $(\sqrt{\pi}h_*/2h_*)B_K = 0.32$. Also, the fraction of total light in K from the spirals, approximately 10%, is smaller than that seen in most other galaxies (Seigar & James 1998). Our weaker spiral arms may result from their scale height being underestimated relative to that of the disk. Such an underestimate could be due to K supergiants dominating the spiral flux density in the GP, or be a consequence of underestimating the dust column density associated with the arms. Our spiral model also renders an estimate of the corotation radius of the Milky Way, which is smaller than other estimates, but gives a ratio $R_C/r_* = 2.9$ consistent with determinations from other spiral galaxies (Grosbol & Patsis 1998).

It is interesting to note that our spiral model is consistent with the dynamical model of the Milky Way's spiral arms constructed by Amaral & Lepine (1997) after a trivial 90° rotation, which has four arms but with two arms dominating. Additional evidence of spiral arms comes from recent results on the star formation history of the solar neighborhood (Rocha-Pinto et al. 2000; Hernandez, Valls-Gabaud, & Gilmore 2000), that indicate an intermittent or episodic star formation rate for the Galactic disk. A periodicity of ~ 0.5 Gyr is suggested by Hernandez et al. (2000), and they point out that this periodicity is consistent with crossing a two arm spiral. Assuming $\Omega_0 = 25 \text{ km s}^{-1} \text{ kpc}^{-1}$, our estimate for the corotation radius, $R_C = 0.83 \pm 0.05 R_\odot$ gives a range of star formation periodicity from 0.5 to 0.9 Gyr for a two arm geometry.

7. SUMMARY

We fitted joint models for the Galactic dust and stellar distributions to the *COBE* FIR and NIR emission. Our dust model has 22 parameters adjusted to fit 173,569 data points, while our parameteric model of the stellar emission has 19 adjusted parameters that fits the large-scale NIR emission features in 304,742 data points.

Our model of the Milky Way has several intriguing results:

1. We find a small scale length for the stars in the Milky Way disk. Our estimate of the stellar radial scale length of the Galactic disk ($0.28 R_\odot$) is shorter than older determinations from NIR data ($0.38 R_\odot$; Kent et al. 1991). It is, however, consistent with recent studies using NIR data, such as *IRAS* point sources ($0.33 R_\odot$; Ortiz & Lepine 1993), DENIS data ($0.27 R_\odot$; Ruphy et al. 1996), the Two Micron Galactic Survey ($0.25 R_\odot$; Porcel et al. 1998), and earlier determinations based on the DIRBE data ($0.35 R_\odot$ [Spergel et al. 1996]; $0.31 R_\odot$ [F98]). It also agrees with analysis of local stellar kinematics ($0.29\text{--}0.36 R_\odot$ [Fux & Martinet 1994]; $0.2\text{--}0.34 R_\odot$ [Bienayme & Sechaud 1997]), including recent use of *Hipparcos* data ($0.29\text{--}0.33 R_\odot$; Dehnen & Binney 1998); however, $0.19\text{--}0.25 R_\odot$ in Bienayme (1999)). Recent studies at visual wavelengths are beginning to con-

verge on a shorter scale length as well ($0.21\text{--}0.36 R_\odot$ [Ojha et al. 1996]; $0.36 R_\odot$ [Gould, Bahcall, & Flynn 1997]), though it is yet far from unanimous ($0.47\text{--}0.94 R_\odot$ [Mendez & van Altena 1998]; $0.43\text{--}0.56 R_\odot$ [Ng et al. 1995]). We note that De Jong (1996) finds that the NIR scale length is 20% smaller than the optical scale length in external galaxies. He argues that this is the signature of inside-out galaxy formation: the outer regions of spiral galaxies are younger than the inner regions. This small scale length has a number of important implications for the Galactic mass distribution: (1) it implies that maximal disk models are a good fit to the Galactic rotation curve (Dehnen & Binney 1998) and implies a low central density for the dark matter halo, which contradicts CDM simulations (Sellwood 2000); (2) it can increase the microlensing optical depth toward the Galactic bulge and will produce more long duration events (Binney, Gerhard, & Spergel 2000; Sackett 1997); (3) it implies that the Galaxy is significantly smaller than our neighbor M31 (Hiromoto et al. 1983).

2. We find that a two-arm spiral structure dominates the NIR nonaxisymmetric emission, supporting the earlier simple analysis of Drimmel (2000). What stellar population dominates our spiral arms in the near-IR? Diffuse NIR emission associated with the spiral arms will have contributions from both young stellar populations, such as K supergiants, and from the old disk population if a spiral density wave is present. The geometry from these two types of populations will not necessarily be the same, as new stars are born from gas subject to hydrodynamic forces. Our standard model of sheared H II arms, that are redder than the disk, is consistent with the assumption of the spiral emission being produced by young K supergiants, while a $m = 2$ logarithmic spiral model with a more open structure and the same color as the disk is consistent with a density wave. The success of these two geometries may indicate a need to include both types of spiral emission. The small scale height of the arms favors the hypothesis of a young population dominating the spiral emission, though the vertical profile of a density wave perturbation in the stars is not known. In external galaxies with active star formation, young stars dominate the spiral arms even in K band, while in other galaxies the K -band light is tracing the older stars and the stellar mass (Rhoads 1998). Once the 2MASS data is available for our spiral arms, we will be able to address this question in our Galaxy.

3. The Galactic warp is here found to start within the Solar Circle and to have different amplitudes for the dust and the stars. If this is indeed the case it is an important clue as to the nature of the warping mechanism, suggesting that hydrodynamic or magnetohydrodynamic forces are important. It may also suggest that the Galactic warp is not a long-lived feature. One mechanism that would cause a short-lived warp is an interaction with one or more companions; this could cause a different response in the gas and stars of the Galaxy. Both the Magellanic Clouds (Weinberg 1995; Weinberg 2000) and the Sagittarius Dwarf (Ibata & Razoumov 1998) have been suggested in this context.

However, there is an important caveat to this last result, namely, that the *only* large-scale vertical distortion present in the Galactic disk is in the form of a warp. That this may be inadequate is suggested by several points. First, the amplitude of the warp in the dust is apparently inconsistent with radio data of H I. Second, the phase of the warp is found here to be less than 1° , a result also found by F98.

Assuming that the location with respect to the Galactic warp is not a determining factor for the existence of observers, the probability of our being this close to the line-of-nodes ($2\phi_w/\pi$) is less than 1 in 100. The minimizing of ϕ_w effectively maximizes the local tilt for a fixed warp amplitude; the presence of other distortions could produce additional tilt in the dust than what would be produced by a warp alone. In addition, there are several features to the adjustment of related parameters that may be pointing to an inadequacy, namely the inability to adjust Z_\odot in the initial FIR fit and the need for a vertical displacement specific to the local dust feature.

These points suggest the alternative interpretation that, in addition to a global warp, there are small-amplitude oscillations affecting the local structure of the gas and dust that are not described in the model. Evidence for vertical displacements within the Solar Circle can be found in the *COBE* data, particularly with regard to residuals at the spiral arm tangents. Hammersley et al. (1999) has also noted evidence that the spiral arms show displacements out of the GP in NIR point source data. It has been noted in numeri-

cal experiments that small amplitude vertical displacements in the disk could result from oscillations excited by Galactic satellites (Edelsohn & Elmegreen 1997), though displacements specific to the spiral arms would have to be of a hydrodynamic nature.

We are entering a golden age for Galactic astronomy. Near-infrared and far-infrared observations are revealing structure that is hidden in the optical. Our analysis here shows that there is a wealth of Galactic structure information in *COBE* two-dimensional data. This data will soon be complemented by a 2MASS inventory of the bright stars in our galaxies. When this structural data is combined with information from the coming generation of astrometric satellites (*FAME*, *SIM*, and *GAIA*), we will finally have a dynamically detailed picture of our home, the Milky Way.

Thanks are extended to Janet Weiland for assistance in installing the UIDL *COBE* data analysis package. The *COBE* data sets were developed by the NASA Goddard Space Flight Center under the guidance of the *COBE* Science Working Group and were provided by the NSSDC.

REFERENCES

- Amaral, L. H., & Lepine, J. R. D. 1997, MNRAS, 286, 885
 Arendt, R. G., et al. 1998, ApJ, 508, 74
 Bahcall, J. N., & Soneira, R. M. 1980, ApJS, 44, 73
 Bienayme, O. 1999, A&A, 341, 86
 Bienayme, O., & Sechaud, N. 1997, A&A, 323, 781
 Binney, J., Bissantz, N., & Gerhard, O. 2000, ApJ, 537, L99
 Binney, J., Gerhard, O., & Spergel, D. 1997, MNRAS, 288, 365
 Blitz, L., & Spergel, D. N. 1991, ApJ, 379, 631
 Burton, W. B., & Hartmann, D. 1994, Ap&SS, 217, 189
 Davies, J. I., Trewella, M., Jones, H., Lisk, C., Madden, A., & Moss, J. 1997, MNRAS, 288, 679
 De Jong, R. S. 1996, A&A, 313, 45
 Dehnen, W. 1998, AJ, 115, 2384
 Dehnen, W., & Binney, J. 1998, MNRAS, 294, 429
 —. 1998, MNRAS, 298, 387
 Djorgovski, S., & Sosin, C. 1989, ApJ, 341, L13
 Draine, B. T., & Lee, H. M. 1984, ApJ, 285, 89
 Drimmel, R. 2000, A&A, 358, L13
 Drimmel, R., & Spergel, D. N. 2001, in ASP Conf. Ser., Galactic Structure, Stars, and the Interstellar Medium, ed. N. Woodward, M. Bicay, & J. Shull (San Francisco: ASP), in press
 Dwek, E., et al. 1997, ApJ, 475, 565
 Edelsohn, D. J., & Elmegreen, B. G. 1997, MNRAS, 287, 947
 Finkbeiner, D. P., Davis, M., & Schlegel, D. J. 2000, ApJ, 544, 81
 Freudreich, H. 1996, AJ, 4268, 663
 —. 1998, ApJ, 492, 495
 Freudreich, H., et al. 1994, AJ, 429, L69
 Frisch, P. 1995, Space Sci. Rev., 72, 499
 —. 1996, Space Sci. Rev., 78, 213
 Fux, R., & Martinet, L. 1994, A&A, 287, L21
 Georgelin, Y. M., & Georgelin, Y. P. 1976, A&A, 49, 57
 Gerhard, O. E., & Binney, J. J. 1996, MNRAS, 279, 993
 Gould, A., Bahcall, J. N., & Flynn, C. 1997, ApJ, 482, 913
 Grauer, A. D., & Rieke, M. J. 1998, ApJS, 116, 29
 Grosbol, P. J., & Patsis, P. A. 1998, A&A, 336, 840
 Hammersley, P. L., Cohen, M., Garzon, F., Mahoney, T., & López-Corredoira, M. 1999, MNRAS, 308, 333
 Hammersley, P. L., Garzon, F., Mahoney, T., & Calbet, X. 1995, MNRAS, 273, 206
 Hauser, M., Kelsall, T., Leisawitz, D., & Weiland, J. 1999, *COBE* Ref. Pub. No. 98-A (NASA/GSFC: Greenbelt)
 Hauser, M. G., et al. 1998, ApJ, 508, 25
 Haywood, M., Robin, A. C., & Creze, M. 1997a, A&A, 320, 428
 —. 1997b, A&A, 320, 440
 Hernandez, X., Valls-Gabaud, D., & Gilmore, G. 2000, MNRAS, 316, 605
 Hiromoto, N., Maihara, T., Oda, N., & Okuda, H. 1983, PASJ, 35, 413
 Humphreys, R. M., & Larsen, J. A. 1995, AJ, 110, 2183
 Ibatu, R. A., & Razoumov, A. O. 1998, A&A, 336, 130
 Kelsall, T., et al. 1998, ApJ, 508, 44
 Kent, S. M., Dame, T. M., & Fazio, G. 1991, ApJ, 378, 131
 Lagache, G., Aberget, A., Boulanger, F., Désert, F. X., & Puget, J. L. 1999, A&A, 344, 322
 Malhotra, S. 1995, ApJ, 448, 138
 Malhotra, S., Spergel, D. N., Rhoads, J. E., & Li, J. 1995, ApJ, 473, 687
 Mendez, R. A., & van Altena, W. F. 1998, A&A, 330, 910
 Ng, Y. K., Bertelli, G., Bressan, A., Chiosi, C., & Lub, J. 1995, A&A, 295, 655
 Ojha, D. K., Bienayme, O., Robin, A. C., Creze, M., & Mohan, V. 1996, A&A, 311, 456
 Ortiz, R., & Lepine, J. R. D. 1993, A&A, 279, 90
 Paresce, F. 1984, AJ, 89, 1022
 Pohlen, M., Dettmar, R., & Lütticke, R. 2000, A&A, 357, L1
 Porcel, C., Garzon, F., Jimenez-Vicente, J., & Battaner, E. 1998, A&A, 330, 136
 Rhoads, J. E. 1998, AJ, 115, 472
 Rieke, G. H., & Lebofsky, R. M. 1985, ApJ, 288, 618
 Rix, H., & Zaritsky, D. 1995, ApJ, 447, 82
 Rocha-Pinto, H. J., Scalo, J., Maciel, W. J., & Flynn, C. 2000, ApJ, 531, L115
 Ruphy, S., Robin, A. C., Epchtein, N., Copet, E., Bertin, E., Fouque, P., & Guglielmo, F. 1996, A&A, 313, L21
 Sackett, P. 1997, ApJ, 483, 103
 Schlegel, D. J., Finkbeiner, D. P., & Davis, M. 1998, AJ, 500, 525
 Seigar, M. S., & James, P. A. 1998, MNRAS, 299, 685
 Sellwood, J. A. 2000, ApJ, 540, L1
 Smart, R. L., Drimmel, R., Lattanzi, M. G., & Binney, J. J. 1998, Nature, 392, 471
 Sodroski, T. J., Odegard, N., Arendt, R. G., Dwek, E., Weiland, J. L., Hauser, M. G., & Kelsall, T. 1997, AJ, 480, 173
 Spergel, D., Malhotra, S., & Blitz, L. 1996, Spiral Galaxies in the Near-IR, ed. D. Minniti & H. Rix (Garching: ESO)
 Taylor, J. H., & Cordes, J. M. 1993, ApJ, 411, 674
 Vallee, J. P. 1995, ApJ, 454, 119
 Wainscoat, R. J., Cohen, M., Volk, K., Walker, H. J., & Schwartz, D. E. 1992, ApJS, 83, 111
 Weiland, J. L., et al. 1994, ApJ, 425, L81
 Weinberg, M. D. 1995, ApJ, 455, L31
 —. 2000, ApJ, 532, 922